



CFD modeling of liquid film reversal of two-phase flow in vertical pipes

Mohamed M. Hussein¹ · A. Al-Sarkhi² · H. M. Badr² · M. A. Habib²

Received: 9 February 2019 / Accepted: 28 May 2019 / Published online: 10 June 2019
© The Author(s) 2019

Abstract

The phenomenon of two-phase flows is characterized by its wide range of presence in nature and industrial applications. In gas and oil production, the simultaneous two-phase flow of gases and liquids often occurs in gas wells. The produced gases flow rate decreases over the years until reaching a critical flow rate when they lose their ability to lift the associated liquids upward and the liquid film reverses direction, which triggers liquid loading. Liquid loading causes the produced liquids to accumulate in the bottom of the wellbore, which causes a high back pressure that reduces the well production rate till production is ceased eventually. The critical gas velocity exists in the churn flow regime which is mainly characterized by the oscillatory behavior of the liquids flow field. This study employs CFD techniques to model the churn flow in a 3-inch-diameter vertical pipe near the critical gas flow rate for different liquid flow rates. This work utilizes the two-fluid Eulerian model along with the RNG (Re-Normalization Group) k - ϵ turbulence model to investigate the behavior of the flow field in a two-dimensional axisymmetric computational domain. Simulations were carried out using the commercial software ANSYS Fluent 18.2 with air and water as the two working fluids. The model results showed a good agreement with the experimental data and proved the mesh and time independence of the model. Oscillatory behaviors of the liquid film flow rate, shear stress, and pressure were observed along with the formation of interfacial waves. Detailed information about the velocity, shear stress, and pressure behaviors is presented. Accordingly, recommendations are suggested for future considerations.

Keywords CFD · Two-phase flow · Churn flow · Vertical pipes · Film reversal

Introduction

Research in the area of two-phase flows continues to be one of the hot research areas due to its wide presence in nature and a broad range of industrial applications. Liquid–gas two-phase flow is widely present in gas wells where gases and liquids flow simultaneously. Most of the time, the present flow regime in a given gas well is the annular flow where gases flow at high velocity in the core region while liquids form a film flowing on the pipe wall. In the upward vertical two-phase flow in a typical gas well, the pressure difference along the pipe is reduced gradually over time which,

in turn, reduces the gas velocity. The gas velocity is kept in continuous reduction till it reaches a velocity where the gases cannot drive the liquids to flow up. Afterward, the liquids start falling and accumulating in the wellbore which progressively reduces the liquids production and eventually results in blocking the flow channel. This imposes a back pressure as the accumulated liquids impeding the flowing of gases. Accordingly, the flow in the wellbore is no more an annular flow and high fluctuations and drop in the production rate are observed. The production rate fluctuation and sudden drop are the first common symptom of what is called “liquid loading” that can be observed and measured. However, the onset of this phenomenon occurs beforehand and is not usually predicted.

The initiation of this entire process that eventually leads to loading the gas well is the reversing of the liquid flow direction from upward to starting falling down, the onset of film reversal. At the onset of film reversal, part of the liquid film flows upward, while the remaining liquids keep flowing downward. Eventually, and after the gas velocity reaches

✉ A. Al-Sarkhi
alsarkhi@kfupm.edu.sa

¹ School of Engineering, University of Guelph, Guelph, ON N1G 2W1, Canada

² Department of Mechanical Engineering, King Fahd University of Petroleum and Minerals, Dhahran 31261, Kingdom of Saudi Arabia

the critical velocity, the entire liquid film starts flowing downward. The present flow regime is the annular flow and its transition to churn flow. Two major methods have been approached to determine the gas critical velocity: entrained droplet movement and liquid film stability.

One way to characterize the critical gas velocity is to consider the momentum balance of the entrained droplets. Turner et al. (1969) were the first to develop a model to compute the critical gas velocity by analyzing the movement of entrained droplets. The authors suggested that the critical velocity is equal to the terminal velocity of a droplet during its free fall. They used the largest droplet size in their analysis which intuitively survives the other drops of smaller sizes from falling. The entrained drop movement model and the continuous film model both were compared to the field data of 106 wells and the entrained drop movement model fitted best to the data as it showed satisfactory results for 66 wells' data. So, Turner et al. gave the critical gas velocity, in SI units, by

$$U_{SG,cr} = 6.556 \sqrt[4]{\frac{\sigma(\rho_L - \rho_G)}{\rho_G^2}} \quad (1)$$

where $U_{SG,cr}$ is the critical gas velocity and ρ donates the density. An initial look at Eq. (1) indicates that the critical velocity depends on the surface tension, gas density, and liquid density. It has been suggested to apply an upward adjustment of 20% because the authors found that the model underestimates the minimum gas flow rate. By applying such an adjustment, additional 11 wells best fitted to the entrained drop transport model. Nevertheless, Turner et al.'s model had the disadvantage of assuming that the droplet shape is perfectly spherical and does not change during the flow. Moreover, the majority of the data fitted to the model were for wells having high wellhead pressure, mainly above 1000 psi.

Coleman et al. (1991) tested the entrained drop transport model of Turner et al. on the field data of gas wells with low wellhead pressure, typically below 500 psi. They concluded that the model accurately predicts the critical gas velocity without the need of the 20% adjustment for low wellhead pressure wells. Moreover, Coleman et al. reported, according to their work, that the results are significantly impacted by the pressure and wellbore diameter, while parameters such as temperature, gravity, and interfacial surface tension have negligible effects.

Nosseir et al. (1997) argued that the reason why Turner et al.'s model had some discrepancies is that they did not take the flow regime into consideration. The authors considered two flow regimes: transition flow regime and highly turbulent flow regime. Each of the two regimes has a different expression of the critical gas velocity. For the highly

turbulent flow, the critical velocity reported by Nosseir et al. is Turner et al.'s equation but adjusted by 21%. Nosseir et al. also reported that adjusting Eq. (1) by 21% reduced the absolute cumulative error from 23.5 to 8.3%.

Unlike Turner et al. (1969), Li et al. (2001) did not assume a spherical shape of a liquid drop. Instead, they suggested that an entrained droplet has the shape of an ellipsoid on which their proposed model is based. The reason for such an assumption is that the pressure difference, under high gas velocity, between the aft and fore of the droplet results in a deformation which converts the spherical droplet into an ellipsoid. Consequently, the drag coefficient, C_D , would be unity unlike the value proposed by Turner et al., 0.44. Hence, Li et al.'s model resulted in a lower critical gas velocity formula, which was validated by comparison with 16 gas wells data in China. However, this model did not consider possible coalescence or separation of droplets.

In (2005), Guo et al. claimed that the model of Turner et al. (1969) did not predict the critical gas flow rate accurately even with the 20% adjustment because it neglected the bottom hole conditions which are more dominant than the wellhead conditions. They developed a new method based on the minimum kinetic energy criterion which requires the gas to reach a minimum value of kinetic energy to carry the droplets up. As a result, they came up with a set of equations which can be solved in an iterative manner to obtain the critical gas flow rate.

Experimentally, Westende et al. (2007) measured the size of droplets at the onset of film reversal using a Phase Doppler Anemometry (PDA). They used a 5-cm-diameter pipe and investigated annular and churn two-phase flow with air and water as the two phases. The authors did not observe any droplets falling, which makes the physical background on which Turner et al. model is based doubtful. Hence, this led the authors to conclude that film instability is what characterizes liquid loading. As previous works did not consider the liquid holdup (the amount of liquid in a gas stream) in their analysis, Zhou and Yuan (2010) proposed a new empirical model that is dependent on the liquid holdup as a major factor in liquid loading. The authors used the gas wells' data provided by Turner et al. (1969) and also used data from Coleman et al. (1991) for validation. The model of Zhou and Yuan consists of a set of two equations with each equation being valid for a specific range of liquid holdup values.

Fadairo et al. (2015) proposed a four-phase gas–oil–water–solid mist flow model and compared it to the field data. The study showed that the model fitted more data points than those fitted by (Taitel et al. 1980; Anderson and Jackson 1967). Later, Bolujo et al. (2017) proposed another improved four-phase model, which fitted more data points than Fadairo et al.'s model.

Other researchers characterized liquid loading by the liquid film stability. Zabarar et al. (1986) were experimentally

able to study the two-phase annular flow and monitoring the film flow. They observed that the liquid film reversed its direction at low gas velocity while the flow was completely co-current at high gas velocity. The wall shear stress, liquid film thickness, and pressure gradient were constantly monitored. Furthermore, they noticed that the shear stress direction is downward when the film was flowing upward, while it was periodically changing its direction after the film reversal.

Belt (2007) studied the phenomenon of the film reversal in a 0.05-m-diameter pipe using water and air as the two phases. He concentrated on studying (1) the interfacial friction as it is the dominant driving force for the liquid film to move upward and (2) explaining the secondary flow in the gas core. Belt (2007) concluded that the roll waves play a significant role in determining the film thickness.

Guner (2012) experimentally investigated the initiation of liquid loading in 3-inch 0°, 15°, 30° and 45° deviated pipes. The author measured the liquid holdup and pressure gradient and adopted the concept of film reversal in characterizing liquid loading. Moreover, she conducted a Computational Fluid Dynamics (CFD) simulation for the vertical pipe case using the commercial software ANSYS® Fluent. Main recommendations included improving the inlet geometry of the CFD simulation, modifying the numerical scheme in the Volume of Fluid (VOF) method to Geo-reconstruction and considering the surface tension in the VOF model.

Similar to the work of Guner (2012), Alsaadi et al. (2015) conducted experiments to investigate the initiation of liquid loading but for a highly deviated 3-inch pipe (60°–88°). They measured the pressure gradient and the liquid holdup for different liquid and gas velocities and determined the critical gas velocity for each case. The author concluded that the critical gas velocity was not always at the point where the pressure gradient is minimum.

Most of the researchers tend to use empirical and mechanistic models to model the key parameters of the flow, such as the pressure drop and the average velocities, due to the simplicity of such approaches compared to others. With the current advances in CFD, numerical simulations provide numerous flow details which are not captured by mechanistic models. Jayanti and Hewitt (1997) employed CFD techniques to estimate the flow field in a liquid wavy film of an annular flow. The study considered a liquid film with a fixed interface profile (including a disturbance sinusoidal wave) on the one side, while bounded on the other side by a moving wall at the speed of a disturbance wave in the direction opposite to the flow direction. The boundary condition at the interface was a fixed interfacial shear stress profile obtained from correlations, whereas the inlet and outlet are constrained by periodic boundary conditions. The standard k - ϵ and the low Reynolds number k - ϵ turbulence models were implemented. Results

showed the low Reynolds number k - ϵ model gave a more accurate prediction of the substrate film Reynolds number than the standard k - ϵ model. According to the results, the authors concluded that laminar flow existed in the substrate region, while turbulent flow dominated the disturbance wave region.

Han and Gabriel (2007) and Han (2005) conducted a CFD numerical simulation of annular flow in order to study the phenomena of liquid entrainment and the effect of disturbance waves on its progression. The one-fluid model with the VOF method implemented in the commercial software Fluent 6.18 was utilized with the RNG turbulence k - ϵ model. The authors identified two entrainment mechanisms that are partially similar in that the growing liquid wave is being sheared off at the crest. The major outcome is confirming the role that the liquid disturbance waves play in the liquid entrainment process.

Kishore and Jayanti (2004) established a new CFD model to simulate gas–liquid annular flow in ducts. The governing equations were developed only for the gas phase with the interfacial effect of the liquid film on the gas taken into account by considering a rough-walled duct. The deposition and entrainment rates were considered by adopting empirical correlations of Govan (1990). The results showed good predictions of the pressure gradient and the film thickness of the steady annular flow, while the variation of the gas density affected the results of the developing annular flow.

Liu et al. (2011) developed a two-fluid model based on the VOF method that included the effect of liquid roll waves. The gas phase was modeled as a homogeneous mixture of pure gas and liquid droplets with no slip between the droplets and the gas. The mass transfer between the liquid and the homogeneous mixture was taken into account by including the appropriate source terms in the governing equations. The study showed good predictions of the pressure gradient, film thickness, and shear stress. The authors noted the significant contribution of wave crests to the entrainment process, which was also observed by Han and Gabriel (2007), Han (2005).

Instead of modeling the two-phase flow using a two-fluid model, the flow can be modeled by utilizing a three-fluid model as implemented in the works of Stevanovic and Studovic (1995), Alipchenkov et al. (2004). In this case, the three distinct phases are the continuous liquid film, the gas stream occupying the core region and the dispersed liquid droplets entrained by the gas. Introducing the third phase to the model results in an additional computational effort, especially with the existence of turbulence, compared to the two-fluid modeling and may lead to further conversion issues.

Vieiro et al. (2013) conducted a CFD study using ANSYS CFX 13.0 to investigate the two-phase behavior of the annular flow near the transition to churn flow. They adopted the homogeneous model in a two-dimensional (2D)

axisymmetric computational domain. Surprisingly, the study over-predicted the pressure drop by as high as 100%.

Modeling the behavior of the liquid film is the key to understand the phenomena of film reversal and liquid loading. Experimentally, it is difficult to observe the precise behavior of the liquid film due to the fact that it covers the channel walls. As formerly discussed, most of the analytical studies concentrated on the force balance for a liquid droplet with the use of field data, with little work spent in the film stability criteria. Recently, there have been no studies tending to improve the analytical approaches for the film stability and liquid drop transport criteria which were initiated by Turner et al. (1969). With the current advances in computational modeling, the concentration is expected to shift to CFD modeling. As a result, very few studies have been recently emerged in modeling the annular two-phase flow using CFD techniques such as the 3D work done by Karami et al. (2014) to simulate liquid loading in a horizontal pipe and the study performed by Han (2005) to investigate the liquid entrainment of annular two-phase flow of water and air in a vertical tube. The ultimate objectives of this study are to perform a CFD simulation to investigate the flow behavior in the vicinity of the liquid film. The study focuses on the characteristics of film reversal in order to examine the flow behavior over the range in which the critical gas velocity exists (the velocity corresponding to complete film reversal).

Problem statement

Consider the geometry shown in Fig. 1 where the gas enters a vertical pipe from the bottom and the liquid is injected laterally. Consequently, at the region above the liquid injection, the air flows in the core region with a thin liquid film flowing on the pipe wall. The main objective of this study is to model the two-phase annular flow with special emphasis on the onset of the liquid film reversal and the complete reversal of that film.

Referring to Fig. 1, gas enters the 3-inch (0.0762 m)-diameter pipe vertically and expands to reach an average

velocity that is equal to the superficial gas velocity before the liquid injection. Beside the gas inlet, extra space is extended a distance of $5D$ downward to allow the liquid to fall when reaching the complete film reversal. At the end of this extended space, the pipe is open to allow the falling liquid (if exists) to leave the domain. The liquid is injected at a height of $5D$ above the gas entrance. A height of $25D$ above the liquid entrance is set to allow the flow to fully develop. However, the fully developed flow is not ascertained due to the transient nature of the system. Due to symmetry around the pipe axis, the problem is modeled as 2D axisymmetric. The present study aims to:

- Computationally model the churn two-phase flow with negligible mass transfer between the two phases.
- Analyze and solve for the velocity field and the shear stress of the flow field.
- Study the conditions of the complete film reversal.

Solution methodology

The objective of this section is to present the model utilized including the governing equations and the closure relations. The two-fluid Eulerian model has been implemented as the governing model of the fluid motion, while the RNG k- ϵ turbulence model for each phase is used to model turbulence.

Assumptions

In order to simplify the problem, the following assumptions were made.

- The flow is 2D axisymmetric and incompressible.
- The mass exchange between the two phases is neglected.
- The flow is transient due to its time dependence.
- The flow regime is turbulent.
- The liquid droplets in the gas phase have an extremely small diameter.

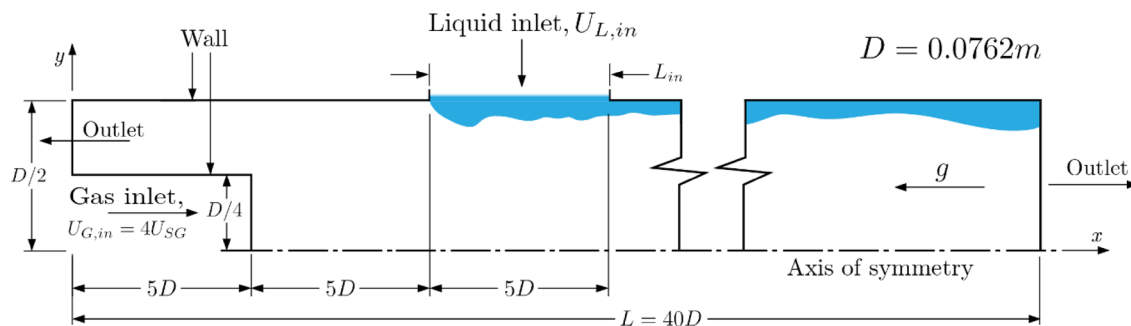


Fig. 1 Schematic diagram of the studied geometry

Governing equations

The conservation equations are derived by time averaging the local instantaneous balance for each phase (Anderson and Jackson 1967) or by implementing the mixture theory approach (Bowen 1976). Each phase has its phase-weighted conservation equations describing its distribution in the domain, velocity field, and pressure variation.

The continuity equations for the liquid and the gas, respectively, are given by

$$\frac{\partial \alpha_L}{\partial t} + \nabla \cdot (\alpha_L \mathbf{V}_L) = 0 \quad (2)$$

and

$$\frac{\partial \alpha_G}{\partial t} + \nabla \cdot (\alpha_G \mathbf{V}_G) = 0 \quad (3)$$

where L and G donate the liquid phase and the gas phase, respectively. \mathbf{V} is the velocity vector and α refers to the volume fraction.

The conservation of momentum for the liquid and the gas, respectively, is governed by

$$\rho_L \left(\frac{\partial}{\partial t} (\alpha_L \mathbf{V}_L) + \nabla \cdot (\alpha_L \mathbf{V}_L \mathbf{V}_L) \right) = -\alpha_L \nabla p + \nabla \cdot (\bar{\bar{\tau}}_{v,L} + \bar{\bar{\tau}}_{t,L}) + \alpha_L \rho_L \mathbf{g} + \mathbf{F}_{D,GL} + \mathbf{F}_{s,L} \quad (4)$$

and

$$\rho_G \left(\frac{\partial}{\partial t} (\alpha_G \mathbf{V}_G) + \nabla \cdot (\alpha_G \mathbf{V}_G \mathbf{V}_G) \right) = -\alpha_G \nabla p + \nabla \cdot (\bar{\bar{\tau}}_{v,G} + \bar{\bar{\tau}}_{t,G}) + \alpha_G \rho_G \mathbf{g} + \mathbf{F}_{D,LG} + \mathbf{F}_{s,G} \quad (5)$$

where p is the pressure, \mathbf{g} is the gravitational acceleration vector, \mathbf{F}_D is the interfacial drag force, and \mathbf{F}_s is the surface tension force. $\bar{\bar{\tau}}_{v,L}$ and $\bar{\bar{\tau}}_{t,L}$ are the viscous shear stress tensor and the turbulent shear stress tensor of the liquid, respectively. Similarly, $\bar{\bar{\tau}}_{v,G}$ and $\bar{\bar{\tau}}_{t,G}$ are the viscous shear stress tensor and the turbulent shear stress tensor of the gas, respectively. The viscous shear stress tensors of both phases are defined as

$$\bar{\bar{\tau}}_{v,L} = \alpha_L \mu_L (\nabla \mathbf{V}_L + \nabla \mathbf{V}_L^T) + \alpha_L \left(\lambda_L - \frac{2}{3} \mu_L \right) \nabla \cdot \mathbf{V}_L \bar{\bar{I}} \quad (6)$$

and

$$\bar{\bar{\tau}}_{v,G} = \alpha_G \mu_G (\nabla \mathbf{V}_G + \nabla \mathbf{V}_G^T) + \alpha_G \left(\lambda_G - \frac{2}{3} \mu_G \right) \nabla \cdot \mathbf{V}_G \bar{\bar{I}} \quad (7)$$

where μ is the dynamic viscosity, λ is the second coefficient of viscosity, and $\bar{\bar{I}}$ is the identity matrix. The formerly stated conservation equations are to be solved for each phase with the interaction term and the continuum surface force term having nonzero values at the interface between the two fluids.

Interfacial drag

The interfacial drag force exerted on liquid phase by the gas phase in general form is given as

$$\mathbf{F}_{D,GL} = \frac{1}{8} \rho_\alpha C_D A_{\text{int}} |\mathbf{V}_{r,GL}|^2 \mathbf{n}_r \quad (8)$$

where A_{int} (the interfacial area concentration), \mathbf{V}_r (the relative velocity vector), \mathbf{n}_r (a unit vector in the direction of the relative velocity), and C_D (the interfacial drag coefficient), according to the symmetric drag model, are given by the following set of equations.

$$A_{\text{int}} = \frac{6\alpha_G \alpha_L}{d} \quad (9)$$

$$\mathbf{V}_{r,GL} = |\mathbf{V}_G - \mathbf{V}_L| \quad (10)$$

$$\mathbf{n}_{r,GL} = \frac{\mathbf{V}_{r,GL}}{|\mathbf{V}_{r,GL}|} \quad (11)$$

$$C_D = \begin{cases} 24(1 + 0.15Re^{0.687})/Re & Re \leq 1000 \\ 0.44 & Re > 1000 \end{cases} \quad (12)$$

Reynolds number and the phase-weighted properties are given by

$$Re = \frac{\rho_\alpha |\mathbf{V}_{r,GL}| d}{\mu_\alpha} \quad (13)$$

$$\rho_\alpha = \alpha_L \rho_L + \alpha_G \rho_G \quad (14)$$

$$\mu_\alpha = \alpha_L \mu_L + \alpha_G \mu_G \quad (15)$$

where d is the length scale which is assumed to be 10^{-5} m. Notice that $\mathbf{F}_{D,GL} = -\mathbf{F}_{D,LG}$. The symmetric drag model is recommended when the secondary phase in a region of the computational domain becomes the continuous phase in another.

Surface tension

Brackbill et al. (1992) CSF (Continuum Surface Force) model is employed to model the surface tension in the current study. It accounts for the surface tension force by adding it as source terms in the momentum equations. Hence, the surface tension force, \mathbf{F}_s , is given by

$$\mathbf{F}_s = C_{LG} \sigma \kappa_L \nabla \alpha_L \quad (16)$$

or

$$\mathbf{F}_s = C_{GL} \sigma \kappa_G \nabla \alpha_G \quad (17)$$

where

$$C_{LG} = C_{GL} = \frac{\alpha_L \rho_L + \alpha_G \rho_G}{\frac{1}{2}(\rho_G + \rho_L)} \quad (18)$$

κ_L and κ_G are the curvatures of the liquid and the gas, respectively, at the interface, and given by the divergence of the normal vector to the interface,

$$\kappa_L = \nabla \cdot n_{n,L} = \nabla \cdot \left(\frac{\nabla \alpha_L}{|\nabla \alpha_L|} \right) \quad (19)$$

and

$$\kappa_G = \nabla \cdot n_{n,G} = \nabla \cdot \left(\frac{\nabla \alpha_G}{|\nabla \alpha_G|} \right) \quad (20)$$

σ is the surface tension coefficient. Note that $\kappa_G = -\kappa_L$ and $\nabla \alpha_G = -\nabla \alpha_L$. The surface tension force is a source term that is added to each of the momentum equations of the liquid and the gas phases. It is split between the two equation based on volume averaging as

$$F_{s,L} = \alpha_L F_s \text{ and } F_{s,G} = \alpha_G F_s \quad (21)$$

In the work of Bartosiewicz et al. (2008), the authors showed that splitting the surface tension force by volume did not result in significant differences with the analytical solution. Hence, it is implemented in the current study.

Interface tracking

Tracking the interface between the two phases is accomplished by solving for the volume fractions of the two phases, α_L and α_G . The volume fraction of the secondary phase, α_L , is obtained by solving the conservation equations, and the volume fraction of the primary phase, α_G , is obtained from the axiom of continuity,

$$\alpha_G = 1 - \alpha_L \quad (22)$$

Turbulence closure

Turbulence disturbance is generated in both phases due to high velocity gradient at the interface, and thus the flow regime is turbulent (Chen et al. 2015). Han (2005) concluded that the RNG k- ϵ turbulence model is the convenient model for such applications since it is adjusted to account for the low Reynolds number effects and because the liquid film region is similar to the flow in the near-wall region. The RNG k- ϵ model for each phase is adopted in this work as it is the most general approach (transport equations are solved for each phase) and as it captures the turbulent interactions between the two phases while being adjusted to capture the low Reynolds

number effects. Detailed transport equations can be discussed in ANSYS Fluent theory guide (Ansys Inc 2009).

Meshing and computational domain

The geometry was created using ANSYS DesignModeler 18.2, and the mesh was constructed using ANSYS Meshing tool. The created mesh structure is as shown in Fig. 2. The general structure of the mesh involves quadrilateral elements with fine meshing in the vicinity of the wall in order to accurately capture the physics of this viscous region and the momentum interaction between the two fluids. However, the element size gradually increases as approaching the pipe centerline in order to save the computational time.

In order to test the mesh independence of the model, three meshes are generated as described in Table 1.

Test matrix

The superficial liquid and gas velocities considered in this study are part of the data Guner et al. (2015) used in their experimental work and are shown in Fig. 3. The test matrix is chosen such that the complete film reversal is expected to be captured within the selected range of superficial velocities, which is in the churn flow region. The exact values of the test matrix are presented in Table 2.

Initial and boundary conditions

The computational domain is initialized from the gas inlet with a velocity equal to the superficial gas velocity. In other words, the domain is initially filled with air flowing at U_{SG} .

Fig. 2 The mesh

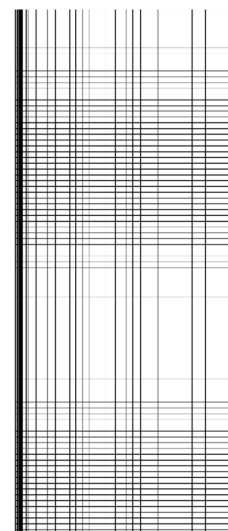


Table 1 Generated meshes

Mesh	No. of elements
1	74,295
2	110,109
3	176,403

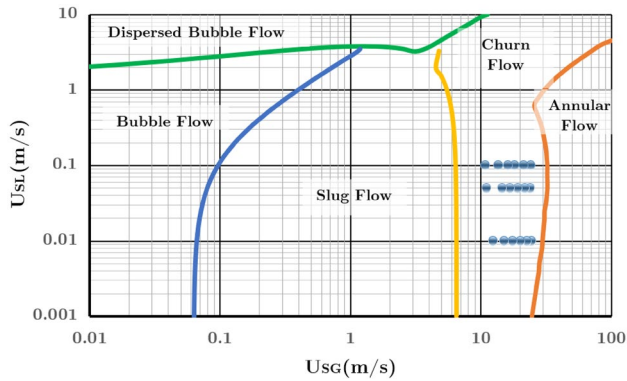


Fig. 3 Input test matrix on the flow pattern map according to the unified model of Barnea (1987)

Table 3 summarizes the boundary conditions implemented. The boundaries of the computational domain are illustrated in Fig. 1, where the inlet liquid velocity and the inlet gas velocity, $U_{L,in}$ and $U_{G,in}$, are given, respectively, by

$$U_{L,in} = \frac{A_P}{A_L} U_{SL} \tag{23}$$

$$U_{G,in} = \frac{A_P}{A_G} U_{SG} \tag{24}$$

where A_L and A_G are the inlet areas of the liquid and the gas phases, respectively. The subscript S denotes superficial. It is significant to mention that since the boundary conditions include two outlet sections, the pressure-outlet boundary condition is not appropriate as it constrains the pressure drop across the pipe length and thus results in an invalid solution. Hence, the outflow boundary condition is implemented to approximate the conditions at the outlet sections.

This study implemented an overall improved geometry and locations of boundary conditions in order to model the actual case of churn flow with film reversal existing at the considered conditions. Hence, the liquid inlet

Table 3 Boundary conditions

Boundary	Condition
Wall	No slips
Liquid inlet	$V_L = U_{L,in} \hat{j}$
Gas inlet	$V_G = U_{G,in} \hat{i}$
Pipe axis	Axis
Top outlet	Outflow
Bottom outlet	Outflow

length is extended such that the liquid velocity at the inlet approaches zero in order to approach the conditions of the actual case and at the same time allowing for complete film reversal. Extending the liquid inlet length along the whole pipe length would make it more justified to logically approximate the liquid inlet region as wall since the velocity would be much smaller. However, it has been found that further extension of the liquid inlet length did not result in a change in the flow field in this region. This improvement in the locations and the geometry of the boundary conditions is implemented in order to obtain a solution that simulates the real actual case of the flow considering there is still so much room for improvement.

Convergence criteria

Problems of multiphase flows do not usually converge to extremely low residuals, such as 10^{-6} . The convergence criteria are set to be 10^{-4} for the default residual parameters and equations: continuity, axial velocities of both phases, radial velocities of both phases, turbulent kinetic energies of both phases, turbulent dissipation rate of both phases and the volume fraction of the secondary phase. Furthermore, the parameters of the mass imbalance, the volume fraction at the outlet section and the average wall shear stress above the level at which the liquid is injected are monitored during the simulation.

Results and discussion

Updated test matrix

Based on the superficial gas and liquid velocities shown in Table 2, the inlet liquid and gas velocities are computed

Table 2 Table of the input test matrix

	U _{SG} (m/s)					
U _{SL} = 0.1 m/s	23.99	21.17	18.03	16.01	13.46	10.72
U _{SL} = 0.05 m/s	23.77	21.77	19.11	16.72	14.44	10.99
U _{SL} = 0.01 m/s	24.23	22.33	19.96	17.41	15.00	12.35

Table 4 Table of the obtained test matrix

	U_{SG} (m/s)					
$U_{SL}=0.1$ m/s	13.26	11.80	10.77	9.29	8.71	6.93
$U_{SL}=0.05$ m/s	12.81	12.15	10.55	9.69	8.37	6.63
$U_{SL}=0.01$ m/s	12.78	11.81	10.80	9.53	8.39	7.06

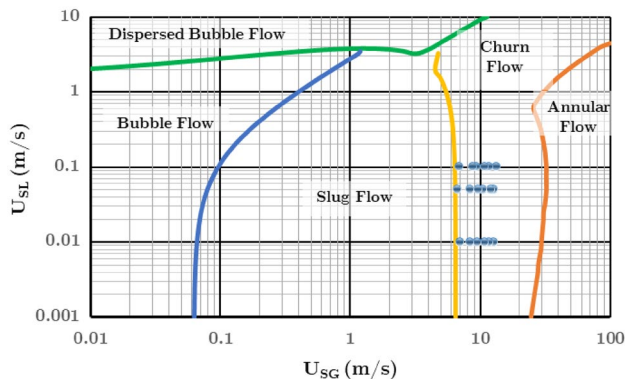


Fig. 4 Obtained test matrix on the flow pattern map according to the unified model of Barnea (1987)

using Eqs. (24) and (23). However, the presence of an outlet at the bottom of the pipe forces some of the gas to leave the domain from the bottom section, which reduces the flow rate of gas interacting with the liquid starting from the liquid inlet. The percentage of the gas leaving the domain through the bottom section ranges from 35 to 47%. Hence, the actual superficial gas velocities are less than those stated in Table 2. Based on the results obtained, the actual gas superficial velocities are depicted in Table 4 and plotted on the flow pattern map as shown in Fig. 4. Note that in this case, the superficial gas velocities are among the obtained results rather than being an input to the model.

Mesh independence

Three different meshes were generated using ANSYS DesignModeler 18.2 in order to verify the grid independence of the model (see “Meshing and computational domain” section for details). The pressure gradient is evaluated for each grid size when $U_{SG}=13.26$ m/s and $U_{SL}=0.1$ m/s and reported in Table 5. Results of mesh 2 and mesh 3 ensure a grid-independent solution. Hence, mesh 2 is selected due to the computational time limitation.

Table 5 Pressure gradient results for different grid sizes ($U_{SG}=13.26$ m/s and $U_{SL}=0.1$ m/s)

Mesh	No. of elements	$-dp/dL$ (Pa/m)
1	74,295	1005.1
2	110,109	981.3
3	176,403	990.6

Table 6 Liquid holdup results for time steps of 0.0005, 0.001 and 0.002 s ($U_{SG}=13.26$ m/s and $U_{SL}=0.10$ m/s)

Time step	H_L	Relative error (%)
0.0005	0.08938	6.1
0.001	0.09742	2.4
0.002	0.10261	7.8

Time step independence

In order to maintain the solution accuracy and yet minimize the computational time, three simulation runs with different time steps (0.0005, 0.001 and 0.002 s) were tested by comparing the resulting liquid holdup H_L with the value interpolated from the experimental study of Guner (2012) (0.09515) and are shown in Table 6.

Guner computed the liquid holdup using two quick closing valves. The liquid holdup of a given two-phase pipe flow is the volume occupied by the liquid within the system relative to the total volume. By knowing the total volume enclosed within the selected domain and evaluating the air volume using the ideal gas law, the liquid holdup is obtained as

$$H_L = \frac{V_L}{V_T} \tag{25}$$

In the current study, the liquid holdup is approximated based on the ratio of the average cross-sectional area occupied by the liquid to the total pipe cross-sectional area within the portion of the domain surrounded by the liquid inlet, which can be mathematically expressed as

$$H_L = \frac{1}{L_{in}} \int_{L_{in}} \frac{A'_L}{A_p} dx \tag{26}$$

where A'_L is the portion of cross-sectional area that is occupied by the liquid. In Eq. (26), L_{in} is taken a bit less than the height of the liquid inlet to avoid the effects of severe film thickness change between the wall and the liquid inlet, $L_{in} = 4.44D$. The film thickness in a given cross section δ is measured horizontally from the wall to the point where $\alpha_L = 0.5$. This approach is shown by Vieiro et al. (2013) to provide a good approximation of the film thickness and adopted by Chen et al. (2015), Yan et al. (2017).

The time step independence test depicted in Table 6 implies the model independence of the time step with relative errors less than 8% for time steps 0.0005, 0.001 and 0.002 s. Hence, a time step of 0.002 s is chosen for the rest of the study due to the computational time limitation.

Model validation

The purpose of this section is to validate the model presented in the proceeding chapter. Hereafter, the study of Guner (2012) is selected as the nominal case. Guner's experiments were conducted for a 3-inch-diameter pipe for a superficial liquid velocity ranging from 0.01 to 0.1 m/s and a superficial gas velocity ranging from 1.5 m/s to 40 m/s for three different inclinations (0° , 15° , 30° and 45°). The computed pressure gradient is compared to Guner's experimental data (Guner 2012) and depicted in Fig. 5. In this study, the pressure gradient is calculated as the average pressure drop along the inlet flow region. The actual behavior of the flow was obtained in the liquid inlet region, as shown in 44.5, since experiments indicated that annular flow does not exist at these conditions. This is why the pressure gradient is calculated at this region and found to be matching with the actual experiment of Guner (2012).

The pressure gradient resulted from the current study shows a good match with the nominal case with a maximum error of 13.4%.

Phase distribution

Figures 6, 7, 8, 9, 10 and 11 show the phase distribution (liquid volume fraction) contours at $t = 10$ s for the cases when $U_{SL} = 0.1$ m/s, $U_{SL} = 0.05$ m/s and $U_{SL} = 0.01$ m/s, respectively. Unless explicitly mentioned, the axial dimension in all the contour plots is scaled down by a factor of 0.15 in order to show the entire length of the pipe and all plots are taken at $t = 10$ s. The phase distribution results show a typical behavior of the churn flow for all the considered cases. Gas occupied most of the pipe core with little liquid entrained captured by the model. Results show that continuous liquid entrainment and deposition take place simultaneously in the vicinity of the liquid–gas interface.

Oscillatory behavior of the formed disturbance waves is observed at the liquid inlet, which is one of the churn flow characteristics. The number of the interfacial waves continuously changes as superposition and separation of these waves occurs continuously. The results indicate that the amplitude of the disturbance waves increases when the gas flow rate is reduced. Along the pipe wall, a wavy liquid film traveling upward covers the pipe wall downstream of the entrance zone. However, at the low liquid flow rate ($U_{SL} = 0.01$ m/s), the amplitude of the interfacial waves was found to be extremely small and becomes more pronounced as the gas velocity increases. In the case of $U_{SG} = 6.93$ m/s and at the lowest considered gas velocity ($U_{SL} = 0.1$ m/s), most of the liquid is observed to flow downward and leave the computational domain through the bottom outlet, while some liquid is

Fig. 5 Validation of the computed pressure gradient versus Guner's experimental data (Guner 2012)

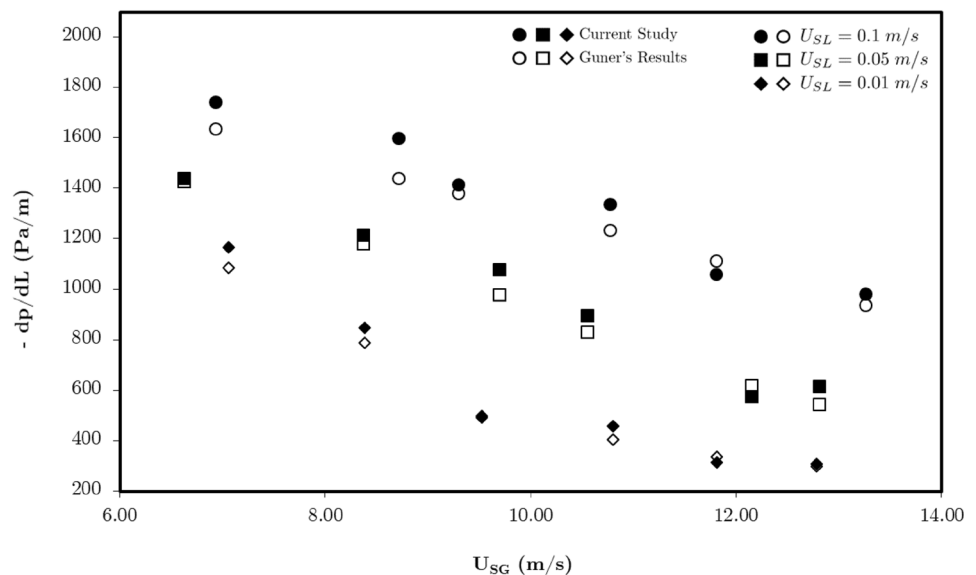
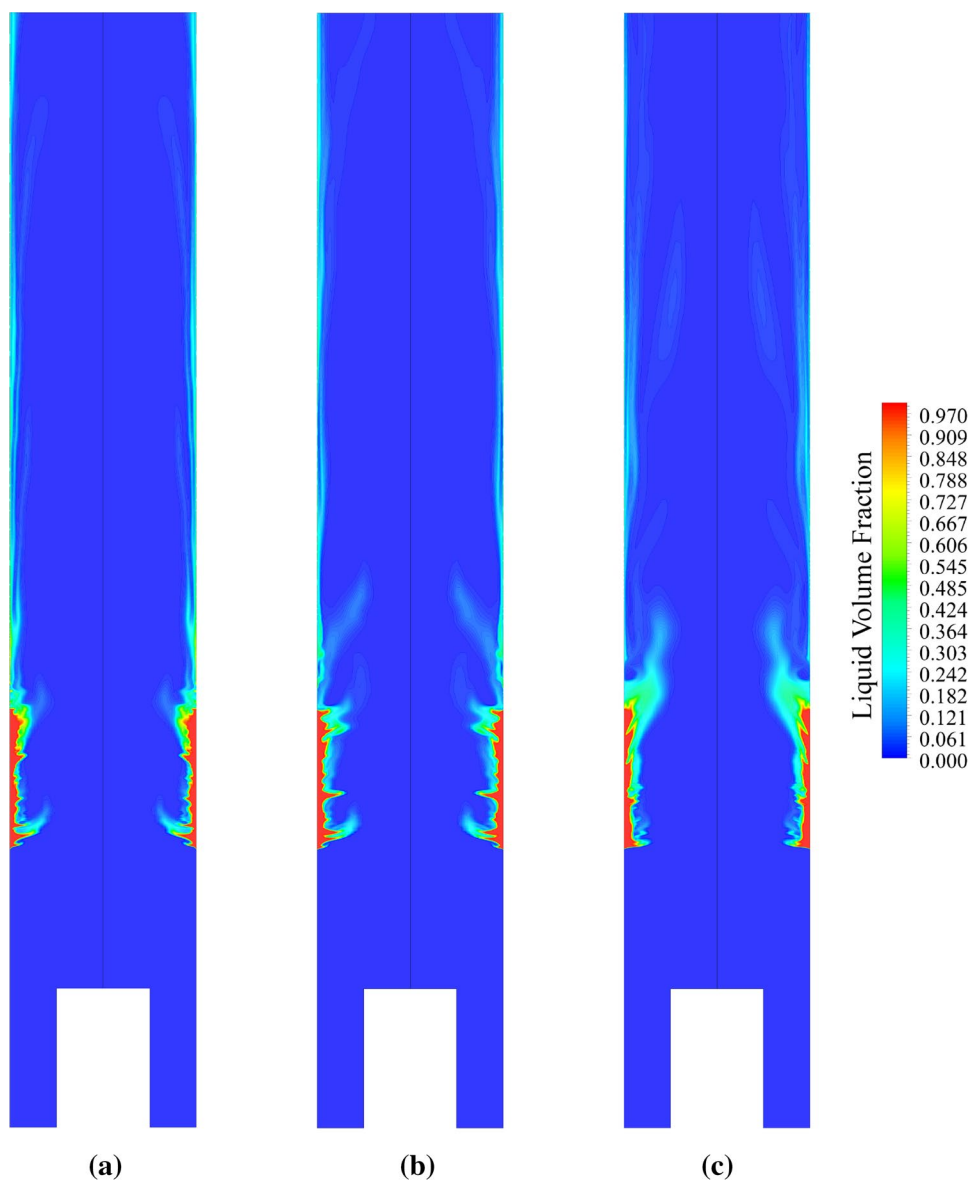


Fig. 6 Phase contour plots of the liquid volume fraction for cases of $U_{SL}=0.1$ m/s and **a** $U_{SG}=13.26$ m/s, **b** $U_{SG}=11.80$ m/s, **c** $U_{SG}=10.77$ m/s



still flowing upward and entrained by the gas, unlike the other cases where the liquid is all discharged from the top outlet.

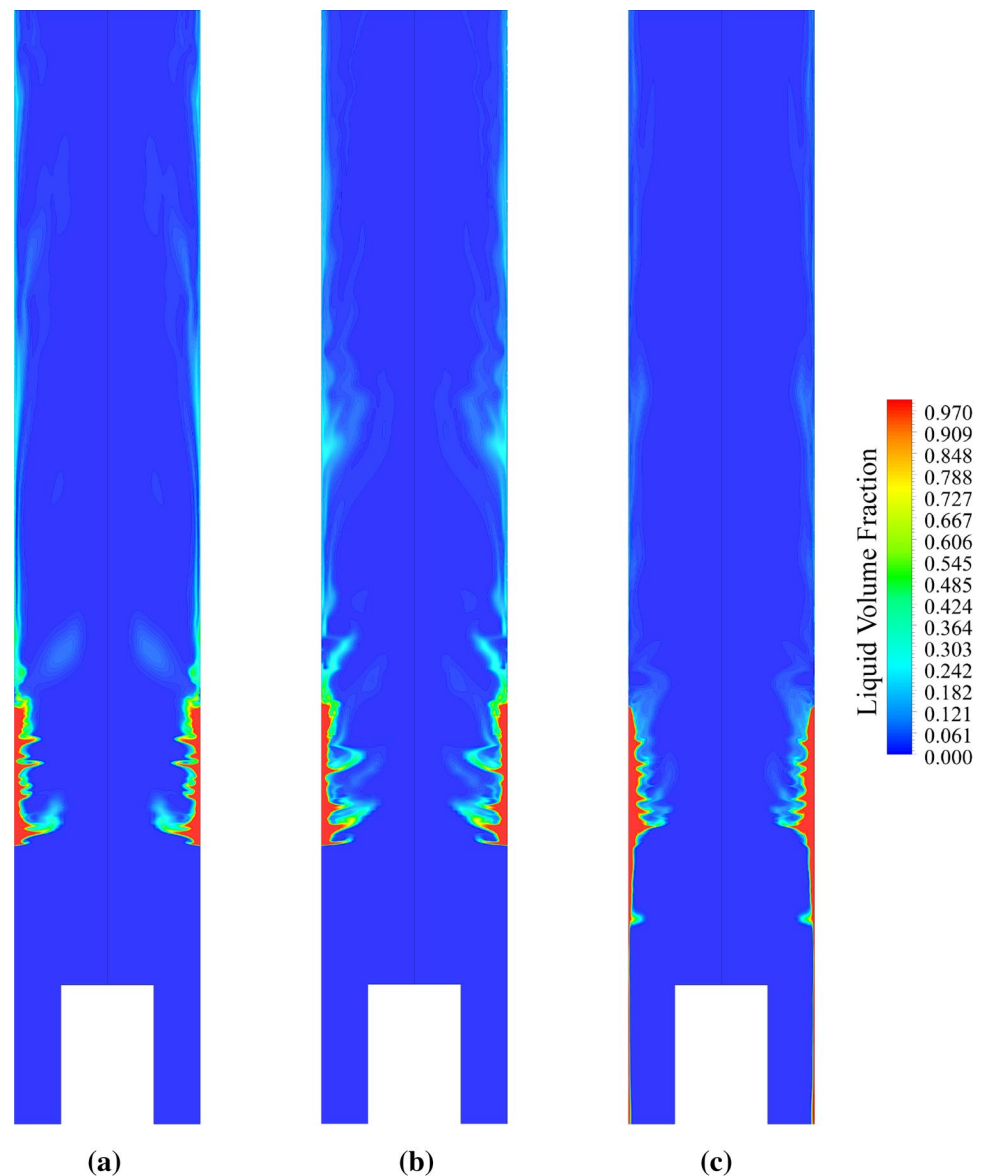
Streamlines

Gas streamlines

Visualizing the streamlines gives key information on the flow structure characteristics. Figures 12 and 13 show the gas streamlines for $U_{SL}=0.1$ m/s contoured with the axial gas velocity for the given range of superficial gas velocities. Several key characteristics of the flow field can be noticed. After the gas enters the flow domain, some of it leaves through the bottom outlet section in a steady manner, while the remaining part flows upward to interact with the laterally injected liquid. As a result of the gas–liquid interactions, the

axial velocity distribution of the gas phase is considerably influenced by the shape of the gas–liquid interface which sometimes forms a nozzle-like shape causing the gas velocity to increase at the nozzle throat followed by the formation of small vortices near the gas–liquid interface. The high shear stress caused by the high gas velocity in the vicinity of the thick liquid layer (throat of the nozzle-like liquid layer) generates interfacial waves due to the abrupt contraction of the turbulent gas flow. Downstream of that region, the gas flow stabilizes with little disturbance resulted from the thin liquid film that keeps the gas streamlines wavy because of its continuous thickness change. However, due to the periodic large entrainment in the liquid inlet region, the streamlines downstream are periodically disturbed. At lower gas superficial velocities, the increased amplitude of the disturbance waves causes a larger rise in the gas velocity near the liquid

Fig. 7 Phase contour plots of the liquid volume fraction for cases of $U_{SL}=0.1$ m/s and **a** $U_{SG}=9.29$ m/s, **b** $U_{SG}=8.71$ m/s, **c** $U_{SG}=6.93$ m/s



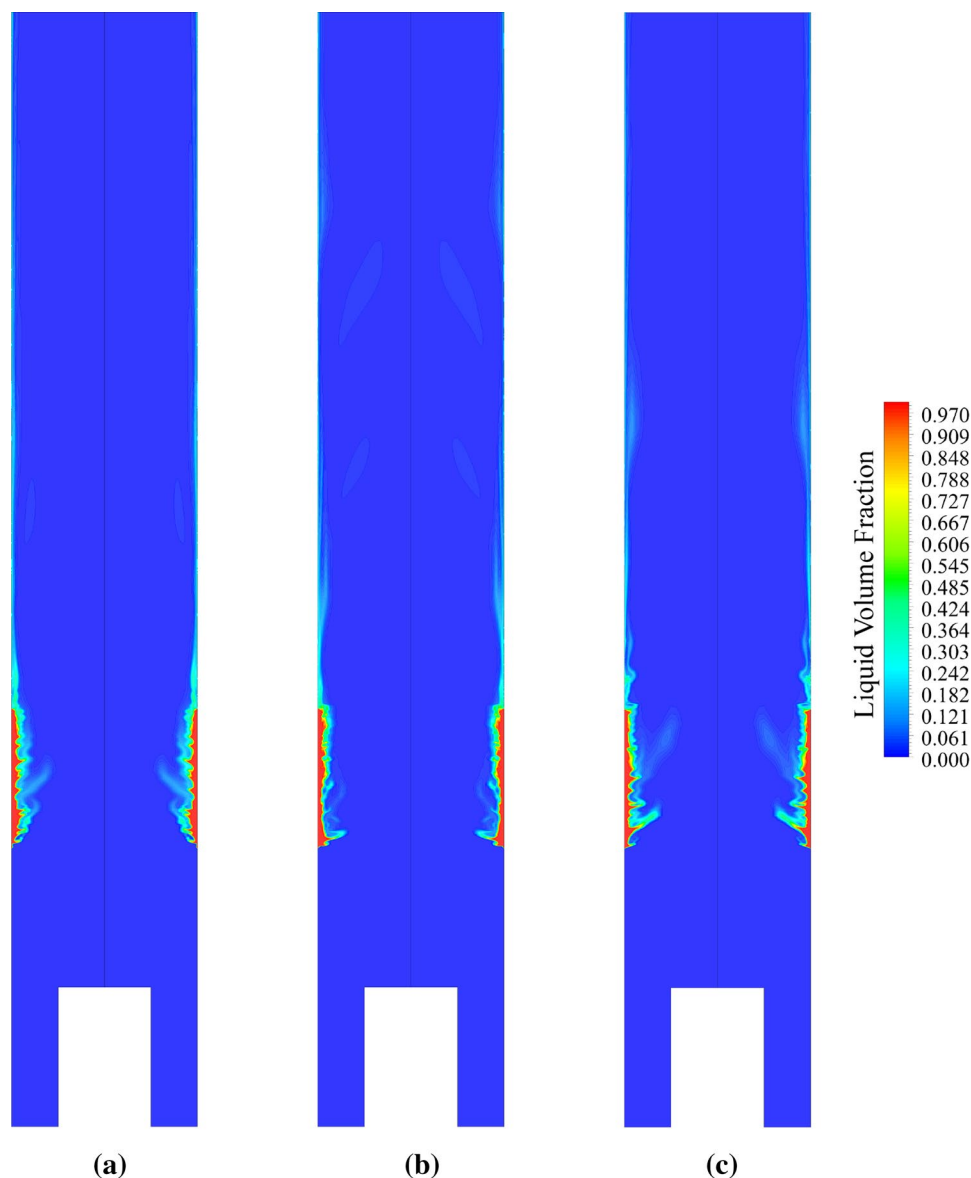
inlet region than that of higher gas superficial velocities. For all cases, except for $U_{SL}=0.1$ m/s and $U_{SG}=6.93$ m/s, the flow below the liquid injection region is steady, but unsteady elsewhere.

Liquid streamlines

The streamlines of the liquid contoured by the axial liquid velocities are shown in Figs. 14 and 15 for the considered range of gas flow rates and $U_{SL}=0.1$ m/s. The figures indicate the presence of liquid vortices near the liquid entrance region. This is manifested by the negative (downward) velocity of the liquid layer in the vicinity of the pipe wall and the positive (upward) velocity near the gas–liquid interface. It is important to mention that the downward velocity near the pipe wall is caused by gravity while the

upward velocity near the gas–liquid interface is caused by the shear stress created by the high gas velocity. In the gas phase, circulating flow regions are also formed due to the curvatures of the gas–liquid interface. The formation of the roll waves phenomenon at the gas–liquid interface may result in the formation of regions of circulation with liquid at the outskirts and gas in the core region. Also, the solution indicated that the resulting gas vortices contain some liquid. The existence of such a phenomenon in a two-phase flow does undoubtedly confirm that churn flow is taking place. Notice that some liquid droplets that have been sheared off by the gas from the crests of interfacial waves rejoin the liquid film again.

Fig. 8 Phase contour plots of the liquid volume fraction for cases of $U_{SL} = 0.05$ m/s and **a** $U_{SG} = 12.81$ m/s, **b** $U_{SG} = 12.15$ m/s, **c** $U_{SG} = 10.55$ m/s



Liquid inlet region

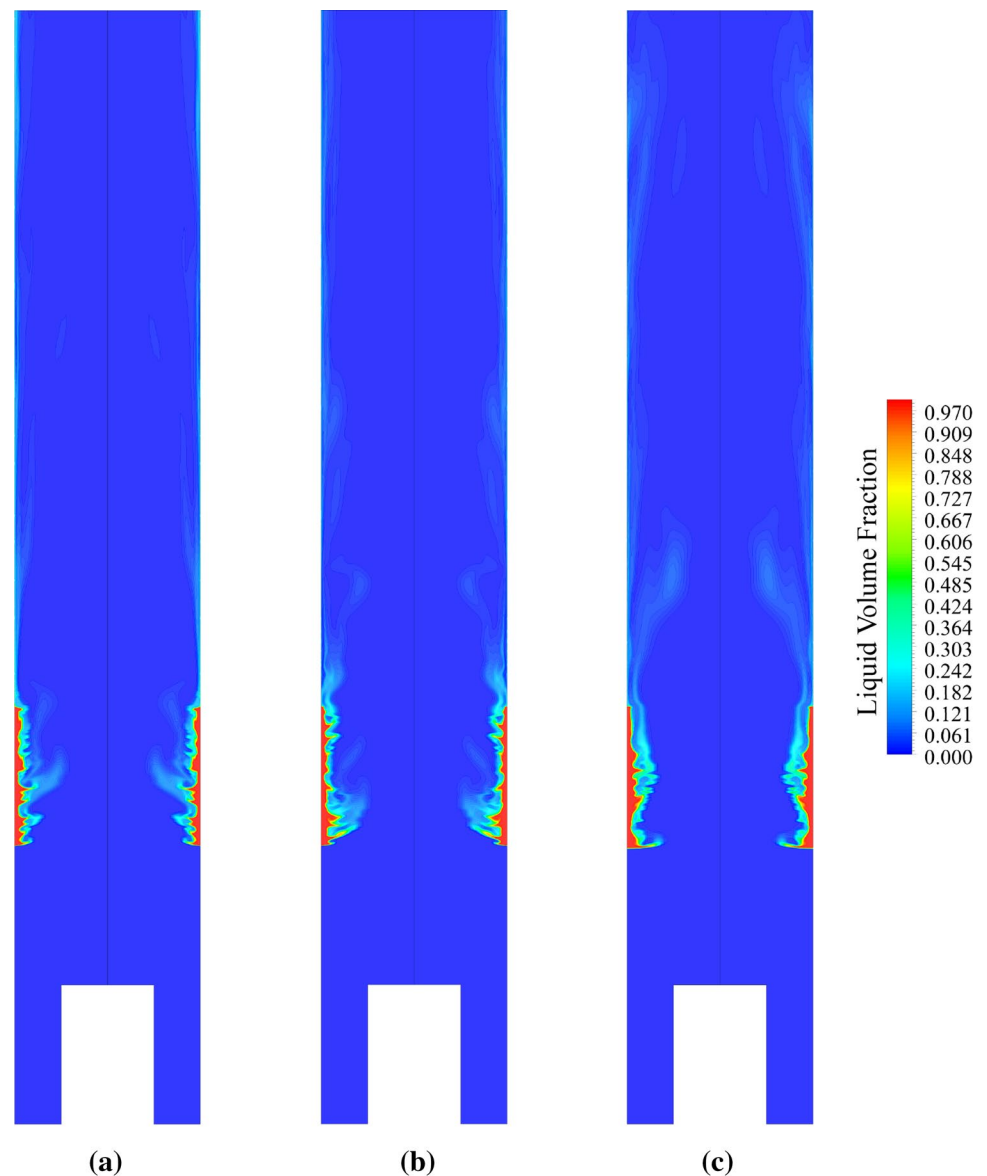
To better visualize the flow field in the vicinity of the liquid inlet region, a zoomed-to-scale contour plot of the gas and liquid streamlines together of the liquid inlet region is shown in Fig. 16a. The figure clearly shows the gas vortices entrained within the liquid film. Moreover, liquid vortices are detected due to the oscillatory behavior of the liquid film. However, because of the unsteady behavior of the liquid film, the axial velocity profiles of both the gas and liquid keep changing continuously.

Figure 16b depicts the velocity vectors near the liquid film. It shows two regions of the liquid film where in the first region (near the pipe wall) the liquid film is moving downward due to both effects of gravity as well as the flow field created by the enclosed gas vortex. In the lower part

of the same region, a stagnation point is clearly visible and separates the upper vortical motion from the lower stream moving upward which is mainly driven by the shearing force at the gas–liquid interface. The above-mentioned interaction between the liquid and gas phases results in the disturbance wave shown in Fig. 16b. The crest of the wave separates from the main film body, thus forming a roll wave that is clearly visible in Fig. 16c. The roll wave phenomenon is normally associated with the formation of a separate liquid droplet that travels with the gas stream and rejoins the liquid layer again at some distance downstream. Some of the separated droplets continue to travel with the gas stream until reaching the discharge section of the pipe.

Figure 16c shows a representative sketch of the flow field in the film region. Axial velocity near the pipe centerline is almost constant due to the turbulent mixing, but it starts

Fig. 9 Phase contour plots of the liquid volume fraction for cases of $U_{SL}=0.05$ m/s and **a** $U_{SG}=9.69$ m/s, **b** $U_{SG}=8.37$ m/s, **c** $U_{SG}=6.63$ m/s



sharply decrease near the interface. The wet gas reverses its direction between the roll wave and the base liquid film, which forms gas vortices.

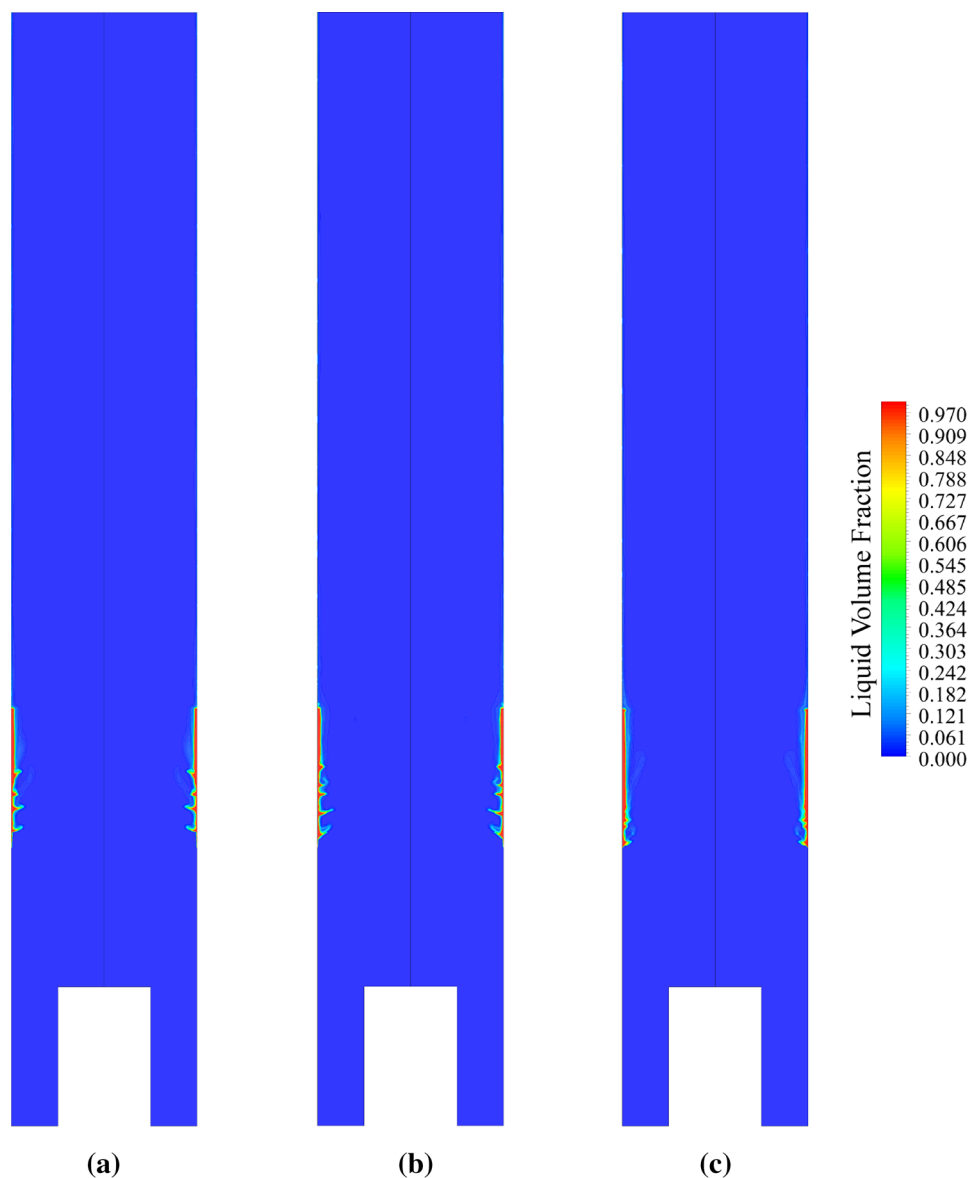
Pressure variation

Due to the various flow phenomena taking place along the pipe, the pressure variation changes accordingly. Figure 17 shows a sample axial pressure profile plot for $U_{SL}=0.01$ m/s and $U_{SG}=11.81$ m/s. The figure shows a sharp rise in the pressure starting from the gas inlet. This is because of the abrupt expansion of the flow passage and the decrease in gas velocity. The pressure rise continues till the gas flow develops just before interacting with the liquid starting from $x=10D$. Within the portion of the domain surrounded by the liquid inlet, the interfacial

waves cause pressure disturbances, and thus a wavy pressure variation takes place. Downstream of the liquid inlet port, the pressure starts to drop in a steady manner due to the very thin liquid film. Notice that a little pressure rise exists just after the flow passes the liquid inlet region due to the drop in the film thickness which gives more cross-sectional area for the gas to flow through.

Moreover, the pressure fluctuates over time due to the variable film thickness, as shown in Fig. 18. When the disturbance wave passes through a given cross section, the pressure drops due to the reduction in the area the gas flows through, whereas the pressure rises again when the wave passes. The pressure keeps oscillating along the pipe except for the steady flow region upstream the liquid inlet port. This fact is furthermore illustrated in the representative Fig. 19.

Fig. 10 Phase contour plots of the liquid volume fraction for cases of $U_{SL}=0.01$ m/s and **a** $U_{SG}=12.78$ m/s, **b** $U_{SG}=11.81$ m/s, **c** $U_{SG}=10.80$ m/s



Shear stress variation

Shear stress variation at the inlet region

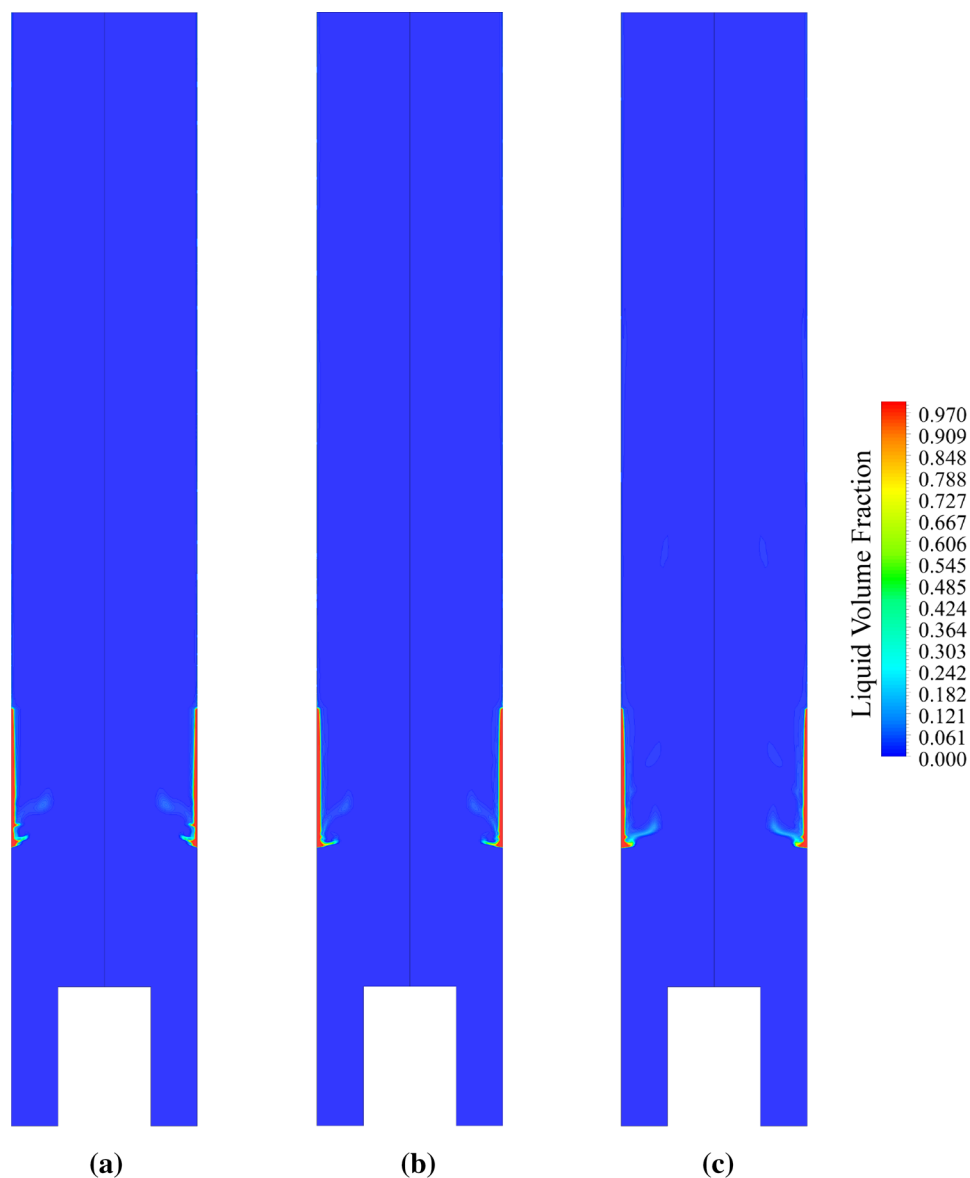
Similar to the pressure space and time variations, the shear stress has a transient oscillatory behavior. Figure 20 shows the liquid wall shear stress in the middle section of the liquid inlet region versus time for $U_{SL}=0.1$ m/s and $U_{SG}=13.26$ m/s. The graph shows a continuous oscillation of the shear stress. However, it oscillates around a positive average value (0.1 Pa) that is close to 0 which implies that the direction of the shear stress exerted on the liquid is upward most of the time. This, in turn, indicates that the liquid on the wall is flowing downward for most of the time. For all the considered cases, the average value is positive.

In addition, the radial distribution of the shear stress is continuously changing with time. Figures 21, 22 and 23 depict the radial distribution of the gas shear stress and the liquid volume fraction in the middle section of the liquid inlet at $t=10$ s for the cases of $U_{SL}=0.1$ m/s, $U_{SL}=0.05$ m/s and $U_{SL}=0.01$ m/s, and different gas velocities in each plot. In these figures, the gas viscous shear stress is defined as

$$\text{Gas shear stress} = \mu_G \frac{\partial v_{x,G}}{\partial y} \quad (27)$$

where the subscript x donates the component along the axial direction. The radial variation of the shear stress shows negative values for most of the radial distance. Starting from the centerline ($y=0$ m), the gas shear stress drops from 0 and bottoms out, and then it keeps undulating as approaching the

Fig. 11 Phase contour plots of the liquid volume fraction for cases of $U_{SL}=0.01$ m/s and **a** $U_{SG}=9.53$ m/s, **b** $U_{SG}=8.39$ m/s, **c** $U_{SG}=7.096$ m/s



liquid inlet port. Furthermore, the magnitude of the fluctuation decreases as the liquid film is approached. The fluctuation stretches closer toward the centerline as the superficial liquid velocity increases. This fluctuation behavior was also observed by Adaze (2018) in the vicinity of the liquid film in his study of CFD annular flow. In some cases, the shear stress takes positive values near the disturbance waves due to the gas vortices.

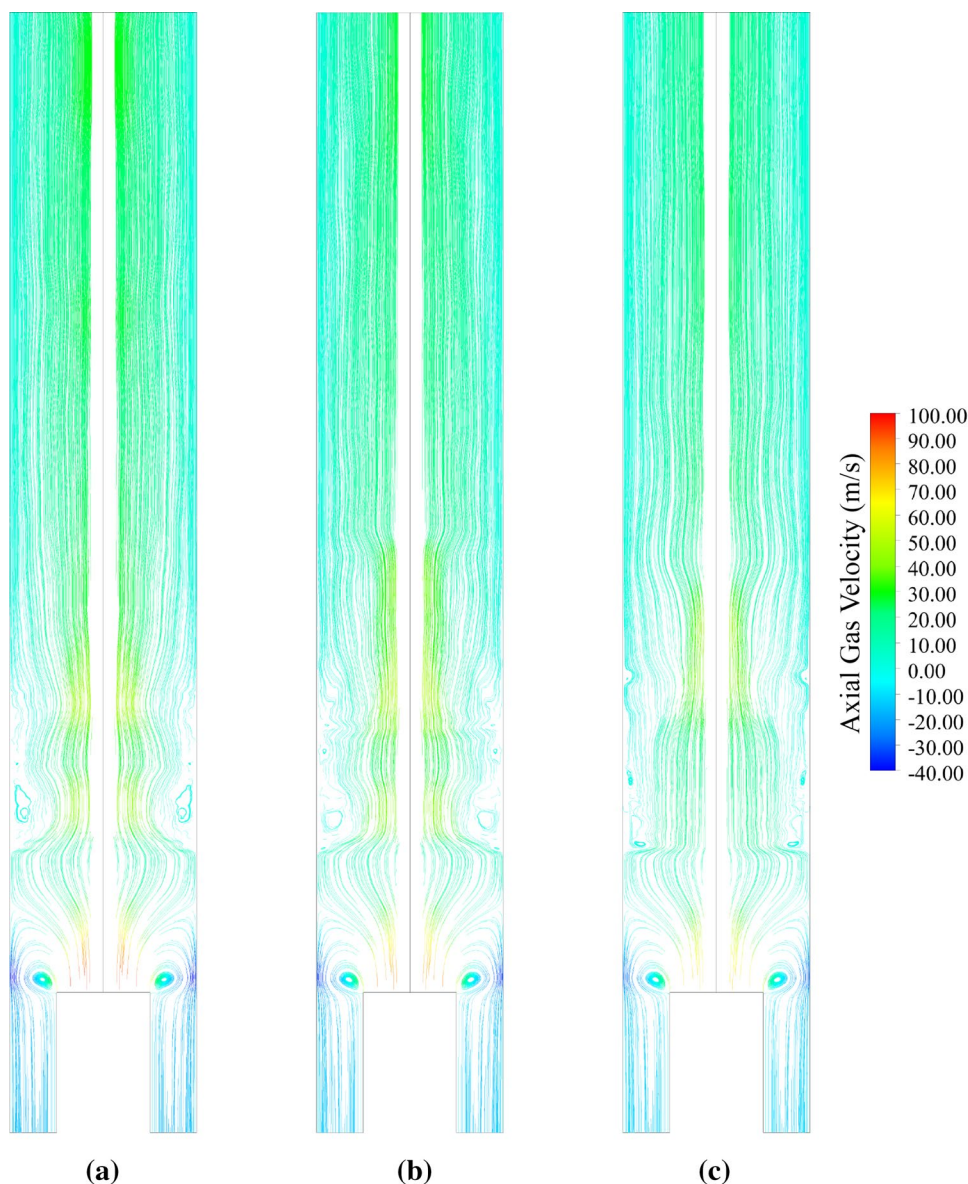
Shear stress variation near the outlet region

Near the outlet section of the flow passage, the flow pattern is mostly annular. Figure 24 shows the liquid wall shear stress at a distance $5D$ before the top outlet versus time for the case of $U_{SL}=0.1$ m/s and $U_{SG}=13.26$ m/s. The figure shows vanishing wall shear stress at small times following

the start of computations due to the absence of liquid near at the wall region. At later time steps, the liquid fills the annular region and the local wall shear stress starts oscillating around a negative value indicating that the direction of the shear stress exerted on the liquid layer is always downward. This, in turn, implies that the liquid on the wall is always flowing upward, which ensures the presence of the annular flow regime.

The radial distribution of the gas shear stress is plotted in Figs. 25, 26 and 27. The figures depict the radial distribution of the gas shear stress and liquid volume fraction at section $x=35D$ when $t=10$ s for the cases of $U_{SL}=0.1$ m/s, $U_{SL}=0.05$ m/s, and $U_{SL}=0.01$ m/s, and different gas velocities in each plot. The radial variation of the shear stress shows negative values for most of the radial distance similar to that at the liquid inlet region. However, their magnitudes

Fig. 12 Gas streamlines contoured with the axial gas velocity for cases of $U_{SL}=0.1$ m/s and **a** $U_{SG}=13.26$ m/s, **b** $U_{SG}=11.80$ m/s, **c** $U_{SG}=10.77$ m/s



of the fluctuation are lower than those observed in the liquid inlet region. A severe rise in the magnitude of the gas shear stress is observed near the pipe wall. This may be attributed to the presence of the viscous sublayer. Furthermore, it is observed that the liquid volume fraction at the pipe wall never becomes unity since most of the liquid is concentrated within the churn flow domain in the vicinity of the liquid inlet port.

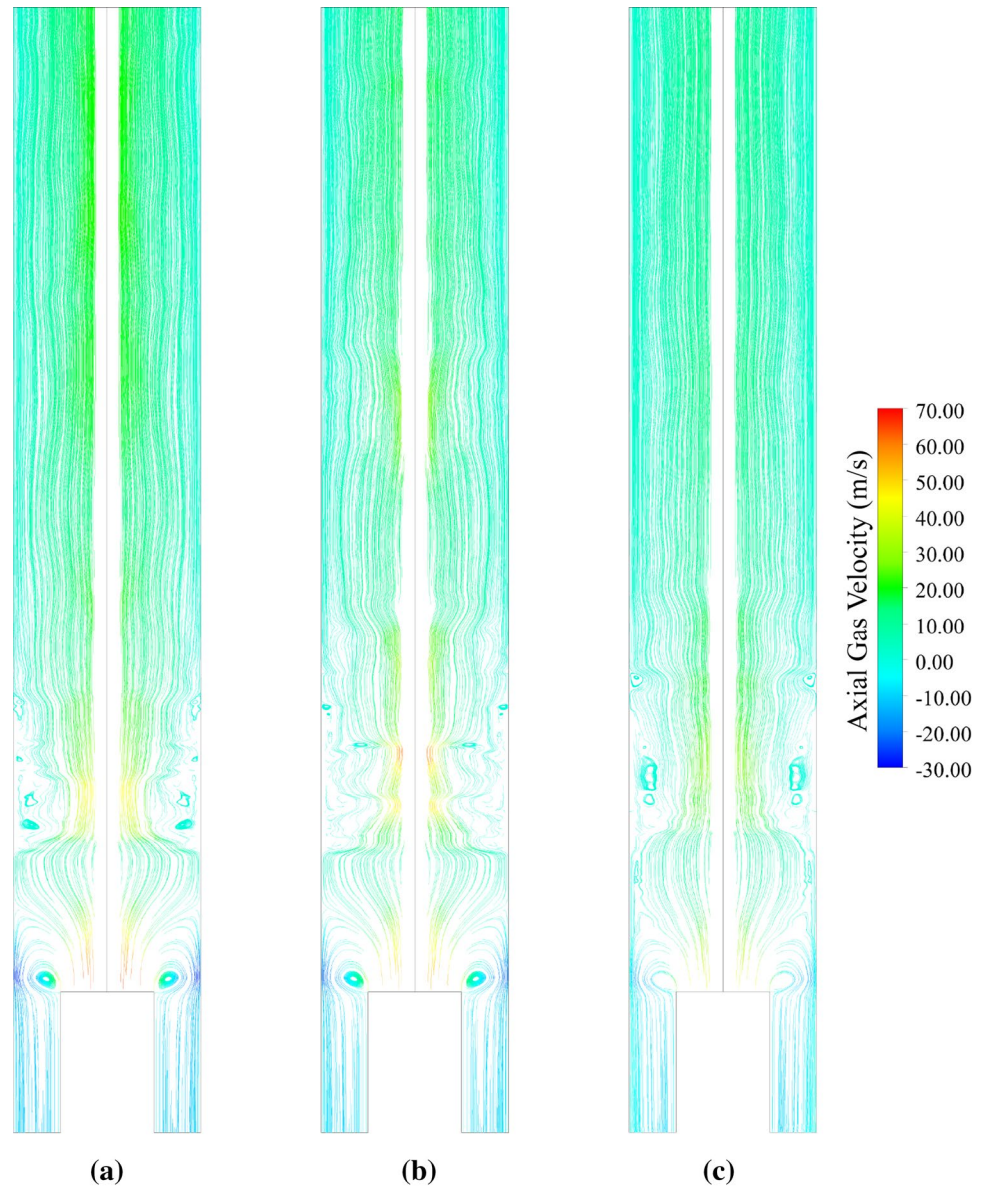
Gas velocity profiles

Gas velocity profiles at the inlet region

Figures 28, 29 and 30 show the gas velocity profiles at section $x = 12.5D$ for cases of $U_{SL} = 0.1$ m/s, $U_{SL} = 0.05$ m/s and $U_{SL} = 0.01$ m/s, respectively. In the core region, the

velocity distribution is almost uniform due to the high mixing of the turbulent gas flow and the exchange of momentum between the gas layers. Near the gas–liquid interface, the gas velocity declines as a response to the interfacial friction caused by the liquid film and the interfacial waves. The velocity profile is continuously changing with time because of the presence of the roll waves, which is by nature an unsteady phenomenon. For a given gas superficial velocity, the gas centerline velocity varies in space and time depending on the geometry of the gas–liquid interface and its axial variation. One can easily see that the maximum gas velocity (centerline velocity) depends not only on the gas superficial velocity but also on the radial velocity distribution that in terms depends on the shape of the local gas–liquid interface. As the film thickness decreases

Fig. 13 Gas streamlines contoured with the axial gas velocity for cases of $U_{SL}=0.1$ m/s and **a** $U_{SG}=9.29$ m/s, **b** $U_{SG}=8.71$ m/s, **c** $U_{SG}=6.93$ m/s



by reducing the liquid superficial velocity, the uniform velocity distribution portion dominates.

Gas velocity profiles near the outlet region

The gas velocity profiles at a distance $5D$ before the top outlet section for all cases are presented in Figs. 31, 32 and 33 for the cases of $U_{SL}=0.1$ m/s, $U_{SL}=0.05$ m/s and $U_{SL}=0.01$ m/s, respectively. It should be emphasized that the velocity profiles are continuously changing with time due to the time variation of the annular liquid layer. Accordingly, the plotted profiles in the above figures represent only samples of the axial gas velocity distributions at time $t=10$ s. The figures indicate that the higher the gas flow rate, the higher centerline gas velocity. Because large amounts of

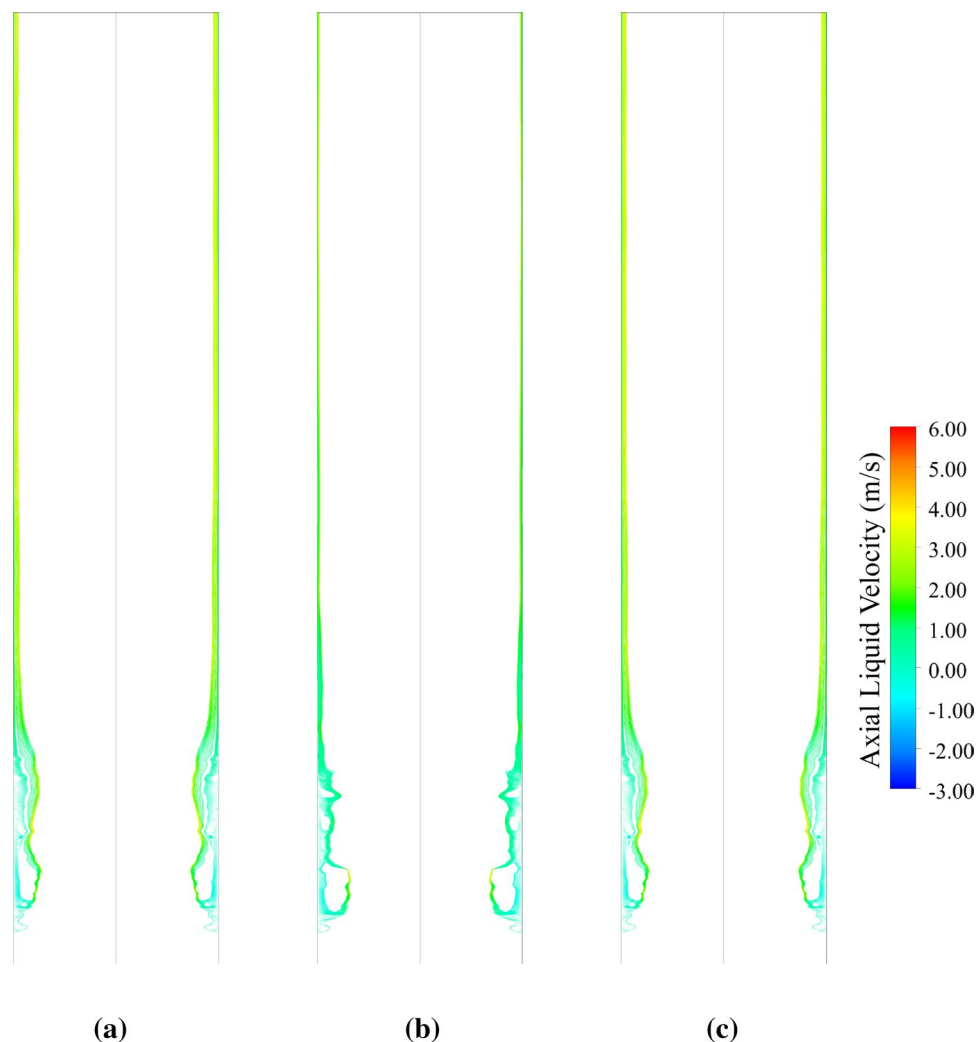
liquid are periodically sheared off by the gas in the liquid inlet region and flowing upward, thus causing a wavy behavior of the gas velocity toward the pipe exit. Figure 33 has the largest number of smooth curves due to the extremely low liquid flow rate.

Liquid velocity profiles

Liquid velocity profiles at the inlet region

Figures 34, 35 and 36 show the liquid velocity profiles at section $x=12.5D$ for the cases of $U_{SL}=0.1$ m/s, $U_{SL}=0.05$ m/s, $U_{SL}=0.01$ m/s, respectively. The liquid axial velocity curves do not extend for the whole radial distance since the liquid does not exist along the whole

Fig. 14 Liquid streamlines contoured with the axial liquid velocity for cases of $U_{SL}=0.1$ m/s and **a** $U_{SG}=13.26$ m/s, **b** $U_{SG}=11.80$ m/s, **c** $U_{SG}=10.77$ m/s



cross section and accordingly $\alpha_L = 0$ in the core region. Some velocity distributions show negative values near the wall indicating the downward flow of the liquid phase. The magnitudes of liquid velocities are similar to those of the gas velocities but with small slip especially when approaching the core region. Liquid entrainment is most pronounced downstream that region.

Liquid velocity profiles near the outlet region

Figures 37, 38 and 39 show the liquid velocity profiles at section $x=35D$ for the cases of $U_{SL}=0.1$ m/s, $U_{SL}=0.05$ m/s and $U_{SL}=0.01$ m/s, respectively. It is clear from the figures that the liquid velocity extends more toward the pipe centerline indicating higher entrainment downstream the liquid inlet port. No negative velocities are observed near the wall and thus no film reversal. By comparing these figures with

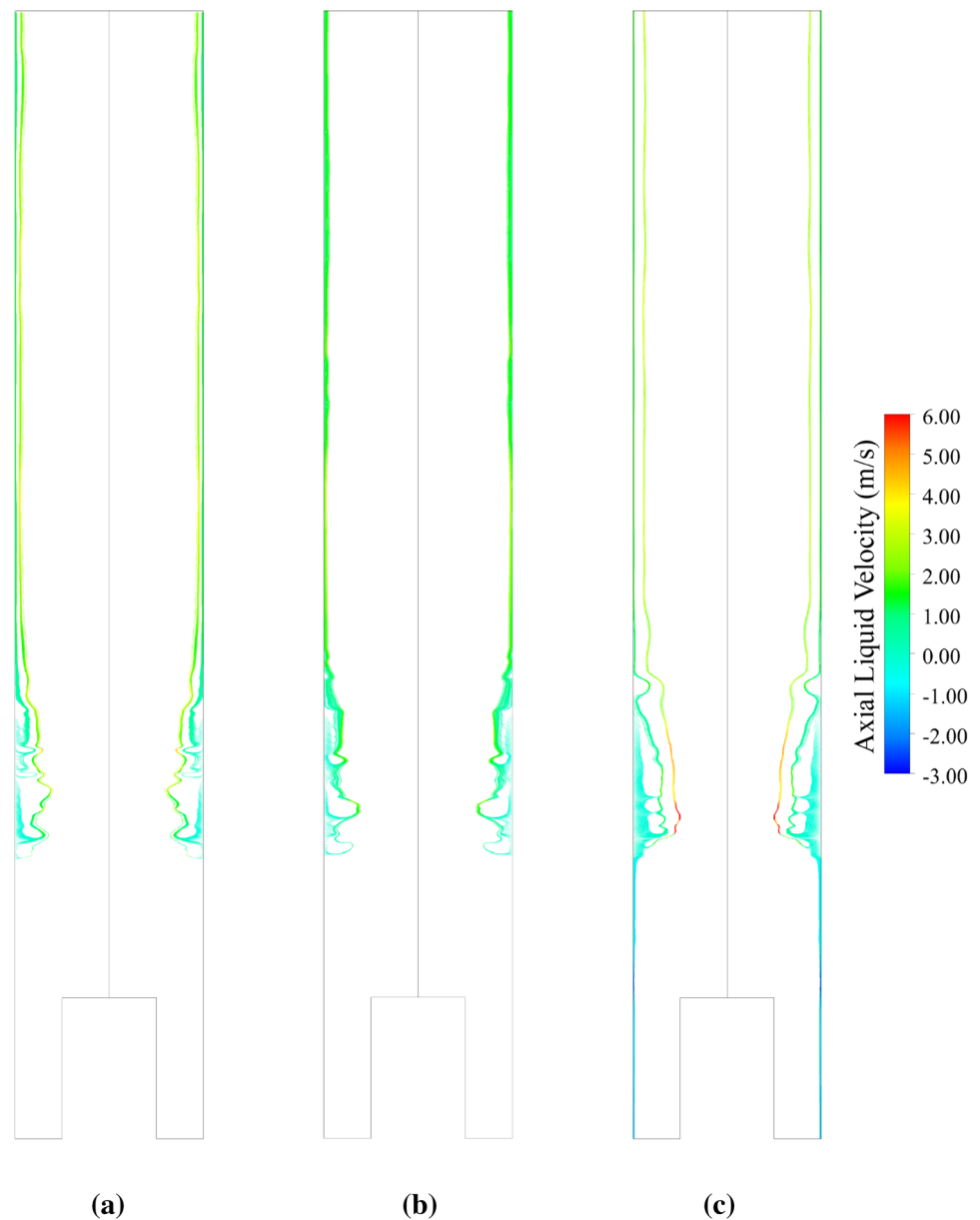
Figs. 31, 32 and 33 of the gas velocity for the same section, the same patterns are observed as the gas velocity ones.

Critical gas velocity

Guner (2012) experimentally determined the gas velocity at the onset of film reversal and the critical gas velocity at the complete film reversal. On the other hand, Adaze (2018) performed a CFD study to investigate the flow field and reported values of the gas velocity at the onset of liquid loading which sufficiently match Guner's results.

According to the current study of churn flow and the shear stress results, the superficial gas velocities corresponding to a complete film reversal are higher than the considered range, i.e., the critical gas velocities for the cases of $U_{SL}=0.1$ m/s, $U_{SL}=0.05$ m/s and $U_{SL}=0.01$ m/s are greater than 13.26 m/s, 12.81 m/s and 12.78 m/s, respectively, which agrees with the results of Guner (2012), Adaze (2018).

Fig. 15 Liquid streamlines contoured with the axial liquid velocity for cases of $U_{SL}=0.1$ m/s and **a** $U_{SG}=9.29$ m/s, **b** $U_{SG}=8.71$ m/s, **c** $U_{SG}=6.93$ m/s

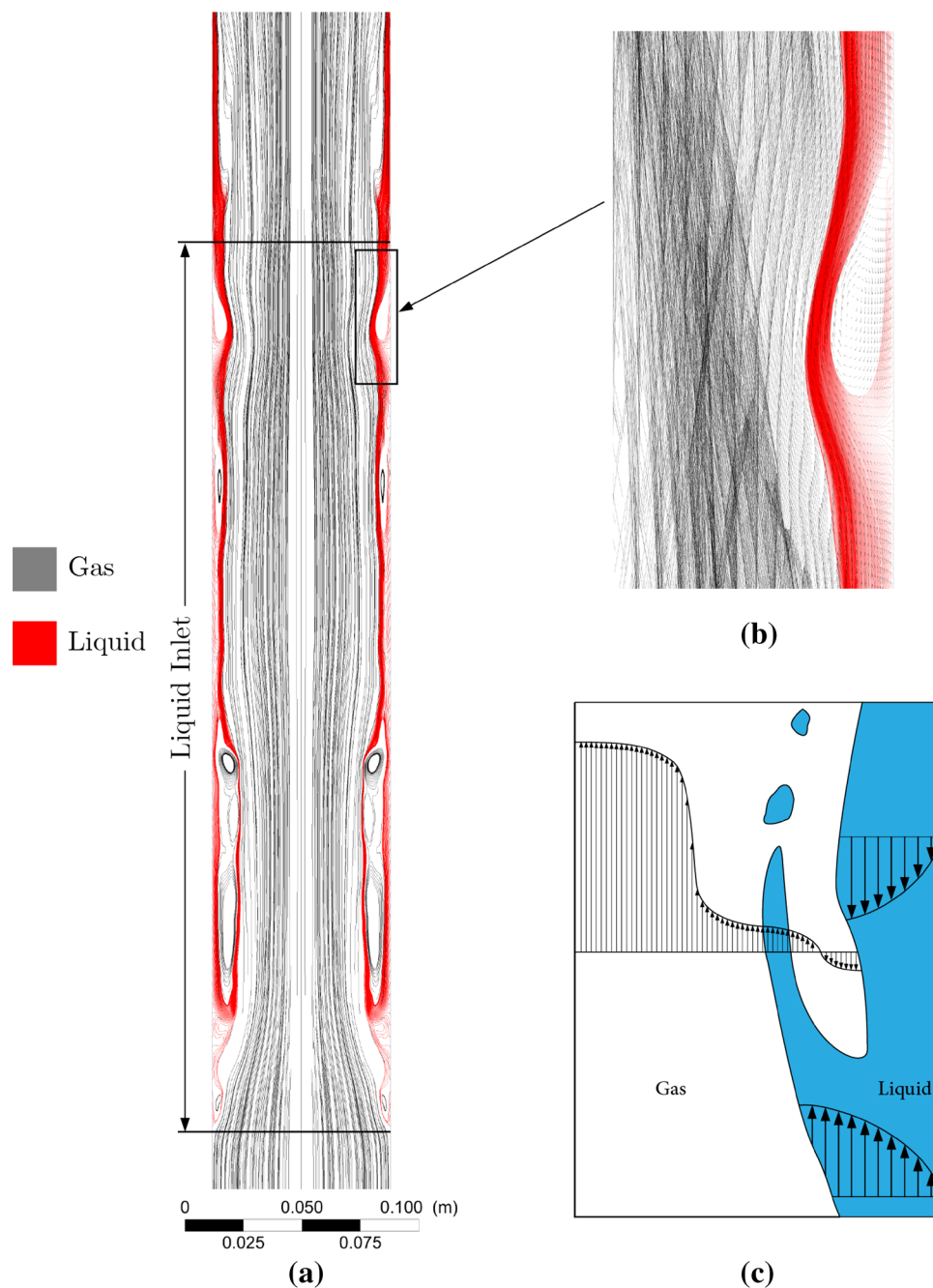


Fluctuation of the liquid wall shear stress around a positive value implies a complete liquid film reversal.

In order to capture the critical gas velocity, cases of higher flow rates are considered ($U_{SG}=13.92$ m/s and $U_{SL}=0.1$ m/s, $U_{SG}=14.58$ m/s and $U_{SL}=0.05$ m/s, and $U_{SG}=15.79$ m/s and $U_{SL}=0.01$ m/s) and the time variation of the liquid wall shear stress for these cases at section $x=12.5D$ is shown in Figs. 40, 41 and 42. It is observed that the liquid wall shear

stress in these cases oscillates around a negative value, which indicates that the average shear stress is downward. Hence, the critical gas velocities are identified as $U_{SG}=13.92$ m/s, $U_{SG}=14.58$ m/s and $U_{SG}=15.79$ m/s for the cases of $U_{SL}=0.1$ m/s, $U_{SL}=0.05$ m/s and $U_{SL}=0.01$ m/s, respectively.

Fig. 16 **a** Liquid and gas streamlines in the liquid inlet region for $U_{SL} = 0.1$ m/s and $U_{SG} = 8.71$ m/s. **b** Zoomed image of the velocity vectors with the liquid streamlines in vicinity of the liquid film. **c** Representative sketch of the velocity profile in the film region



Conclusion

In summary, the current work presents a CFD modeling of churn flow in a 3-inch vertical pipe near the critical gas flow rates. The study implements the two-fluid Eulerian model along with the RNG k - ϵ model for each phase using the commercial software ANSYS Fluent 18.2 (2009). Surface tension is included and the symmetric drag model is adopted for the interfacial momentum exchange.

The axisymmetric geometry was generated by ANSYS Design Modeler 18.2, and the mesh was constructed by ANSYS meshing tool. The geometry and the boundary condition are improved in order to model the liquid film reversal of the two-phase flow involved. The conservation equations were solved using the finite volume method embedded in the software with a convergence criterion set to 10^{-4} for all involved PDEs.

Fig. 17 Sample pressure variation plot along the pipe centerline for the case of $U_{SG}=0.01$ m/s and $U_{SL}=11.81$ m/s

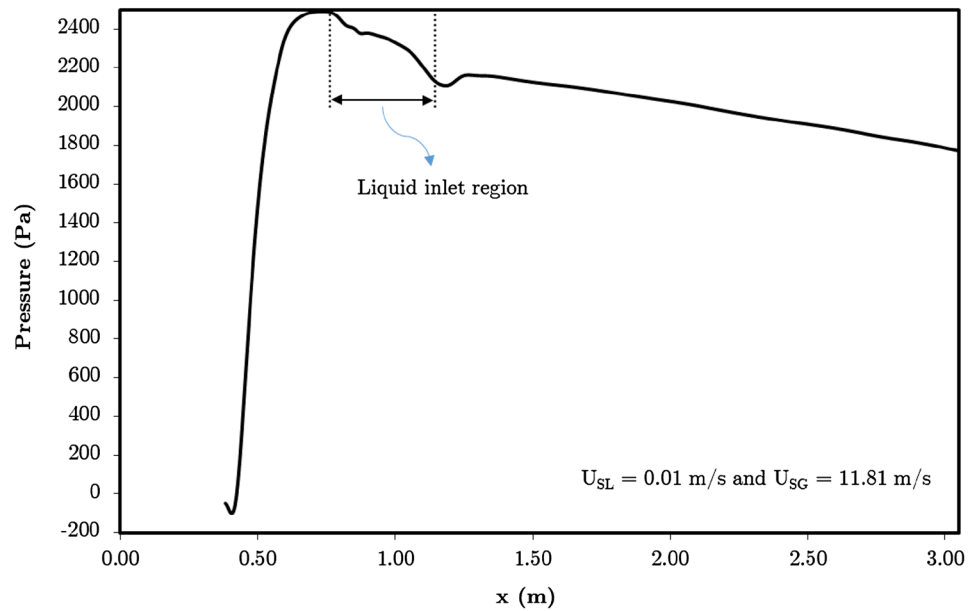
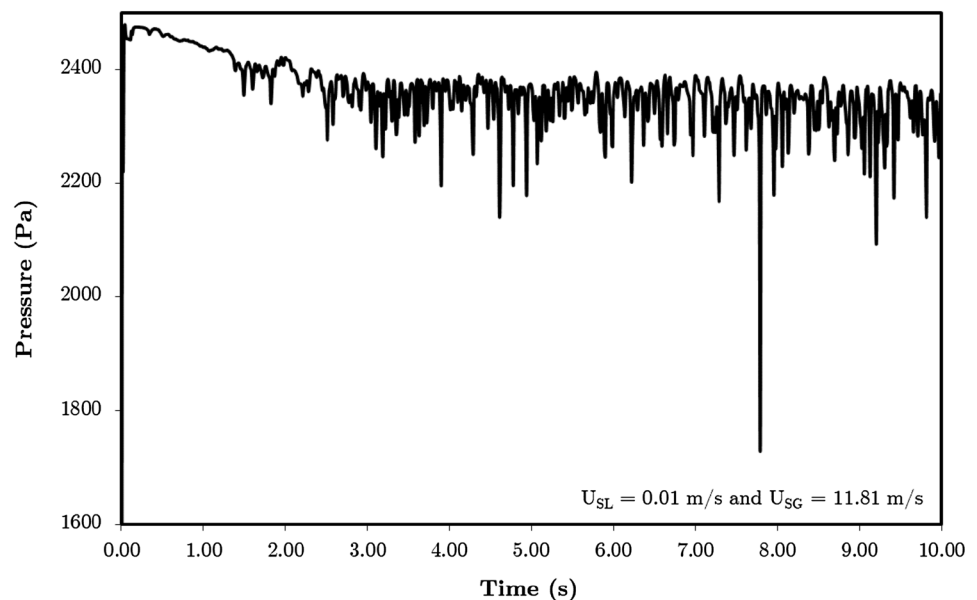


Fig. 18 Sample pressure fluctuation over time on the pipe centerline at section $x=12.5D$ for the case of $U_{SL}=0.01$ m/s and $U_{SG}=11.81$ m/s



Validation curves of the model showed a good agreement with the nominal case. The conclusions of this research include the following:

- The model sufficiently captured the flow field and the nature of churn flow including the interfacial waves, the oscillatory behavior of the liquid, and the pressure and shear stress fluctuations.
- The computational domain surrounded by the liquid inlet port shows the actual characteristics of the churn flow, while the domain above this area is mainly annu-

lar flow with a thin liquid film. Consequently, the liquid holdup is accurately predicted by the model within the domain near the liquid inlet port.

- The interfacial waves play a significant role in disturbing the velocity, shear stress, and pressure fields. Their presence retains the flow unsteadiness. Moreover, the simultaneous processes of liquid entrainment and deposition are highly activated by the disturbance waves.
- Radial fluctuations of the axial gas velocity and shear stress become more pronounced and affected by the disturbance waves as the film thickness increases.

Fig. 19 Representative sketch for the pressure rate of change affected by the interfacial waves

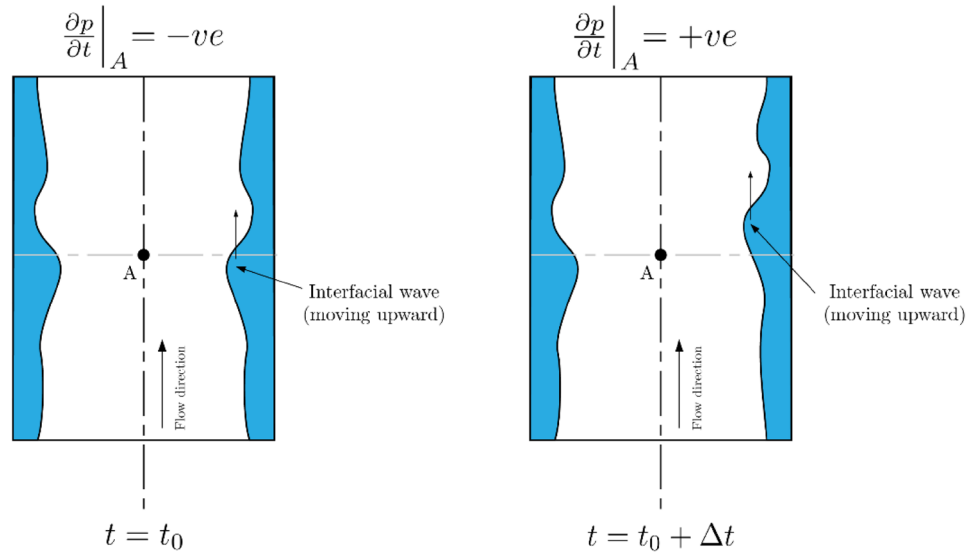


Fig. 20 Sample of liquid wall shear stress fluctuation with time at section $x = 12.5D$ for the case of $U_{SL} = 0.1$ m/s and $U_{SG} = 13.26$ m/s

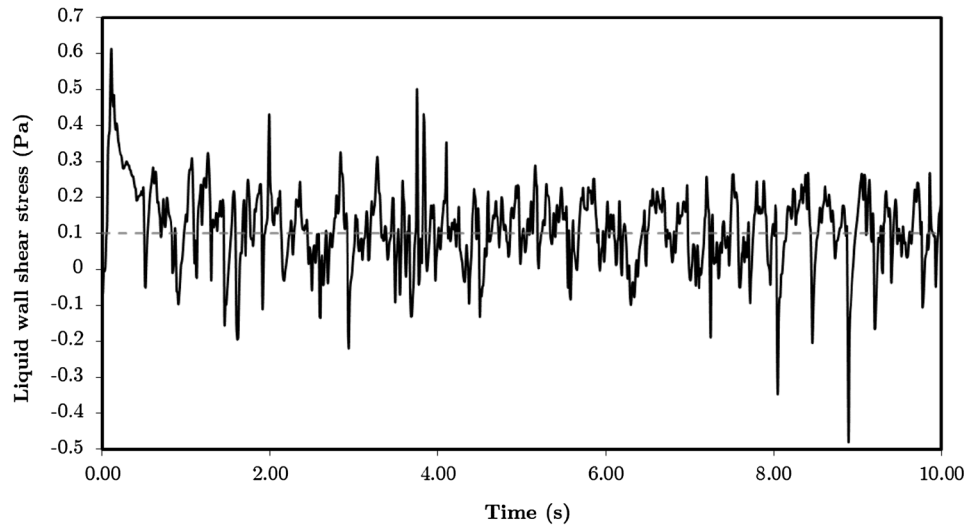


Fig. 21 Radial distribution of the gas shear stress at section $x = 12.5D$ for cases of $U_{SL} = 0.1$ m/s

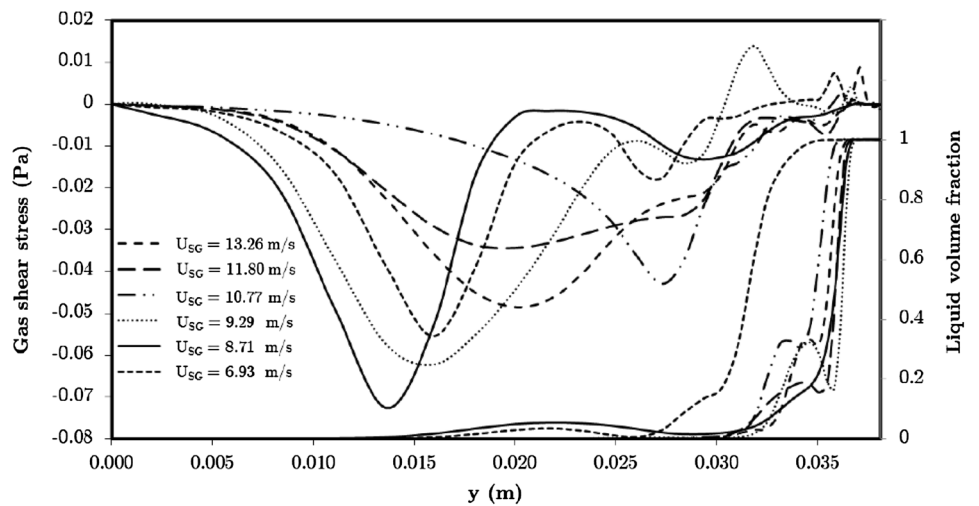


Fig. 22 Radial distribution of the gas shear stress at section $x = 12.5D$ for cases of $U_{SL} = 0.05$ m/s

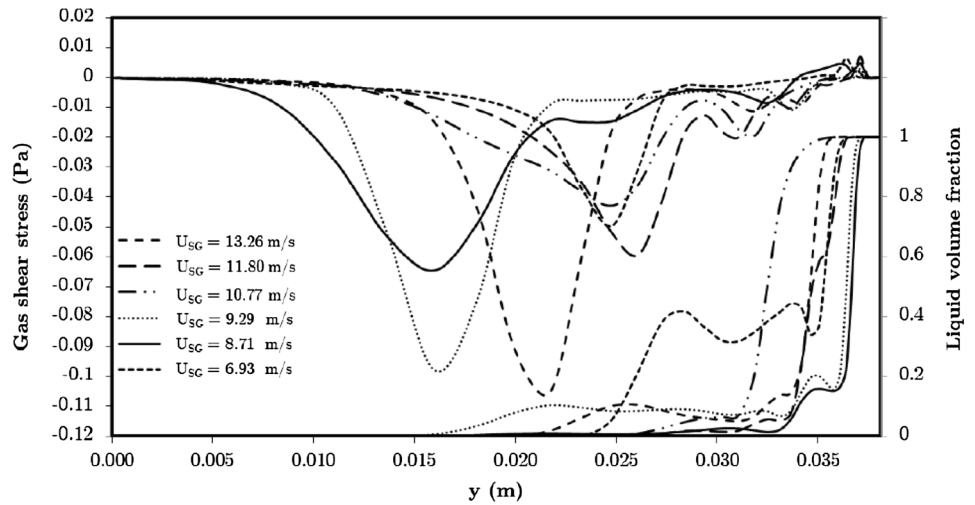


Fig. 23 Radial distribution of the gas shear stress at section $x = 12.5D$ for cases of $U_{SL} = 0.01$ m/s

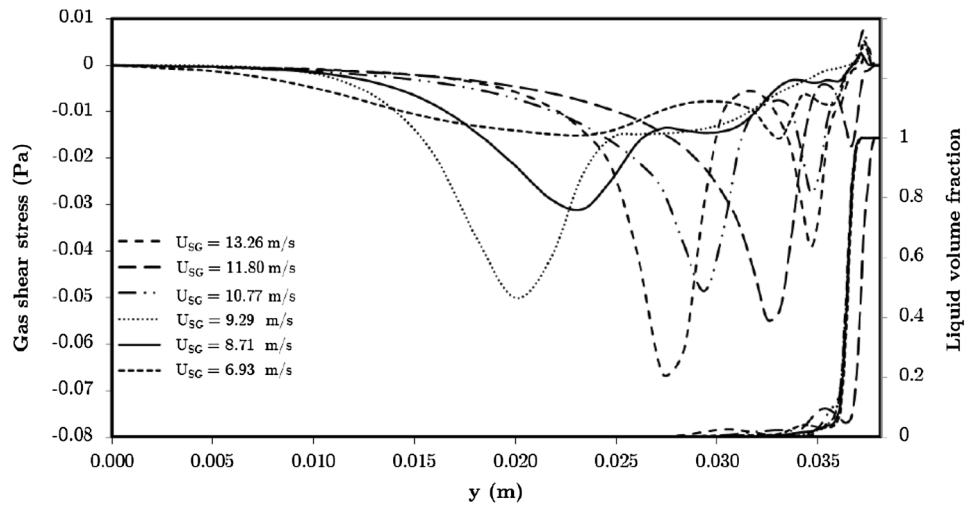


Fig. 24 Sample of liquid wall shear stress fluctuation with time at section $x = 35D$ for the case of $U_{SL} = 0.1$ m/s and $U_{SG} = 13.26$ m/s

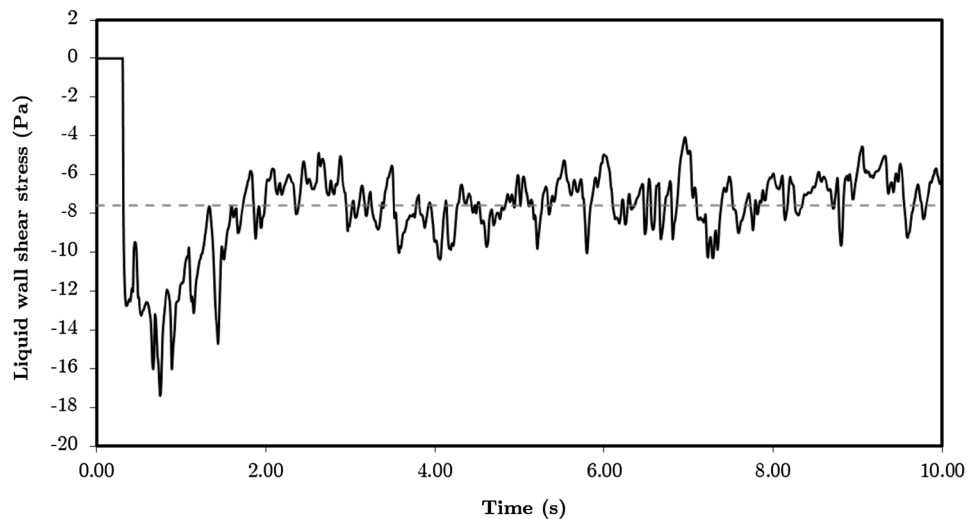


Fig. 25 Radial distribution of the gas shear stress at section $x=35D$ for cases of $U_{SL}=0.1$ m/s

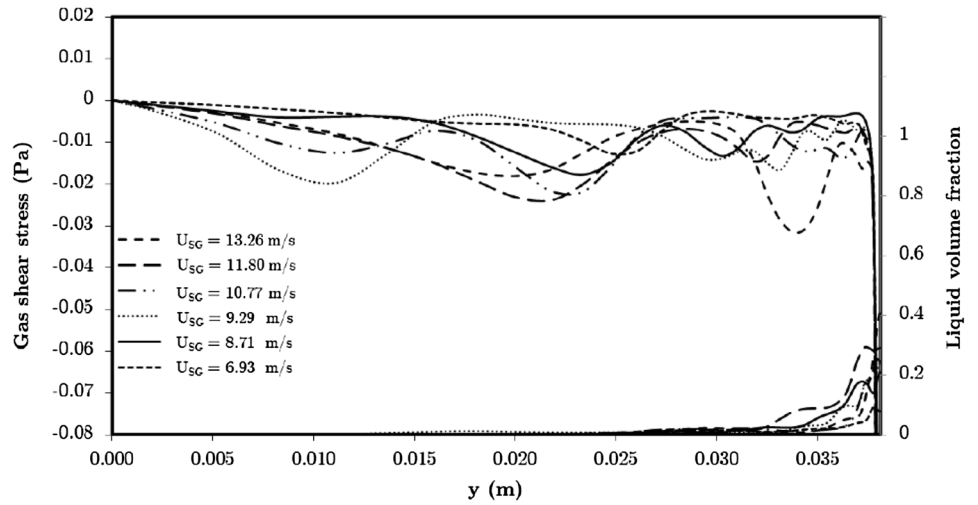


Fig. 26 Radial distribution of the gas shear stress at section $x=35D$ for cases of $U_{SL}=0.05$ m/s

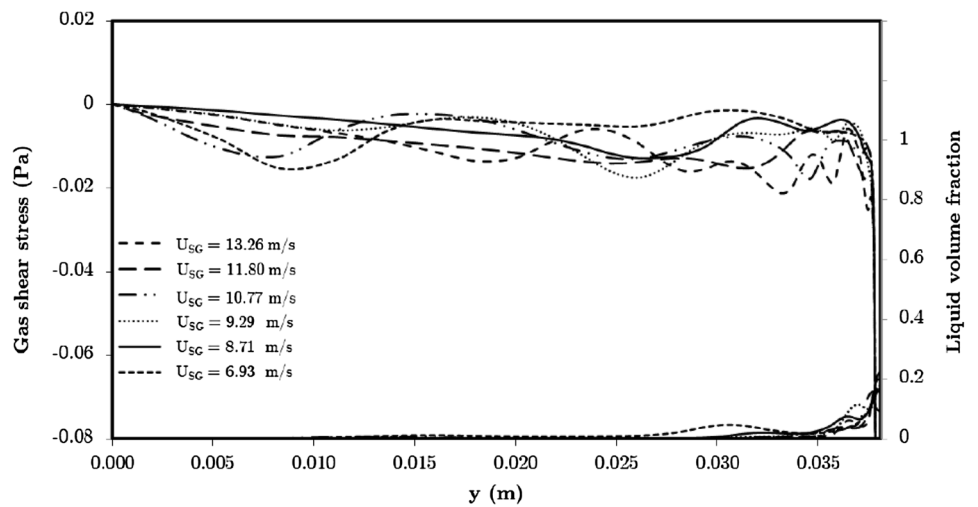


Fig. 27 Radial distribution of the gas shear stress at section $x=35D$ for cases of $U_{SL}=0.01$ m/s

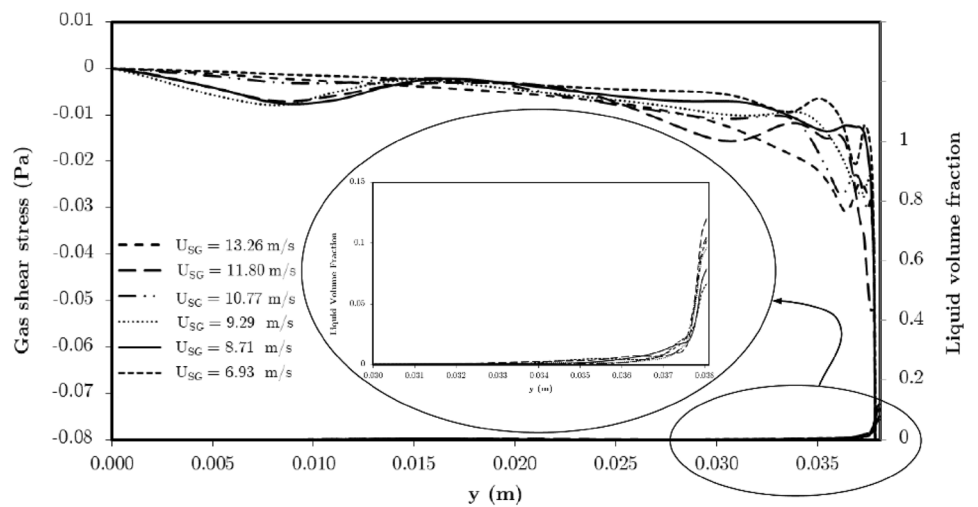


Fig. 28 Radial distribution of the axial gas velocity at section $x = 12.5D$ for cases of $U_{SL} = 0.1$ m/s

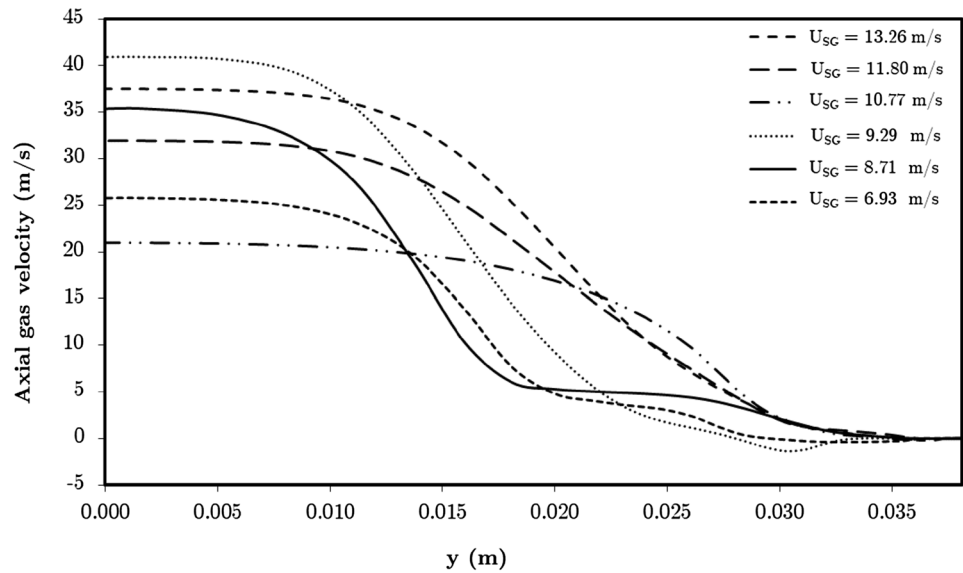
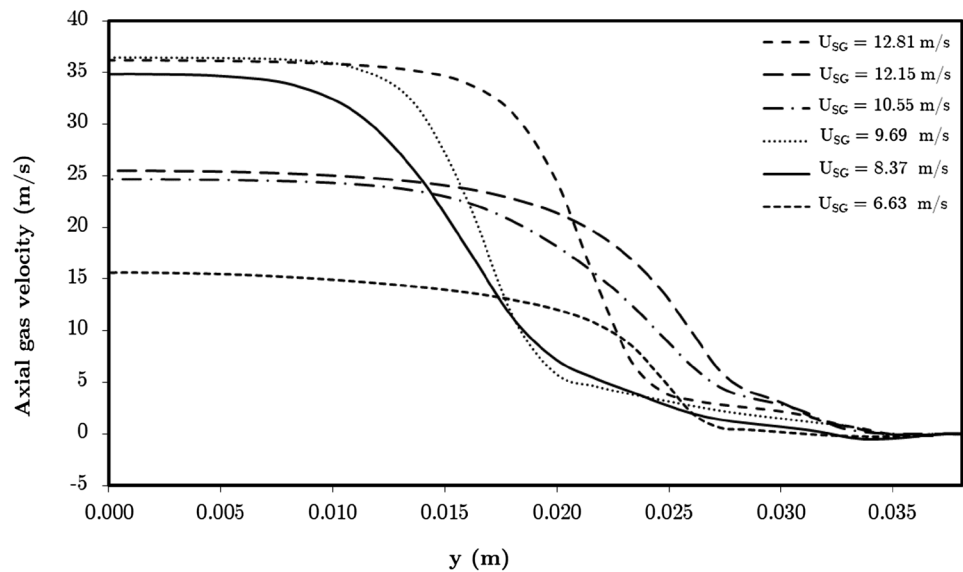


Fig. 29 Radial distribution of the axial gas velocity at section $x = 12.5D$ for cases of $U_{SL} = 0.05$ m/s



- Gas and liquid vortices are observed in the vicinity of the liquid film. Nevertheless, the liquid film is flowing downward most of the time in the middle section of the liquid inlet region.
- According to the shear stress transient behavior, the critical gas velocities are in agreement with what has been reported by Guner (2012), Adaze (2018), i.e., all the considered cases of gas velocities lay below the critical gas velocities except the cases presented in "Critical gas velocity" section.

Nevertheless, for the purpose of further improvements and future studies, the following is recommended to be considered:

- A three-dimensional domain can be considered to more accurately capture the flow details and observe the non-uniformity of the liquid film thickness in the angular dimension.
- The turbulence model is extremely critical and can significantly affect the results. Therefore, the selection of the

Fig. 30 Radial distribution of the axial gas velocity at section $x = 12.5D$ for cases of $U_{SL} = 0.01$ m/s

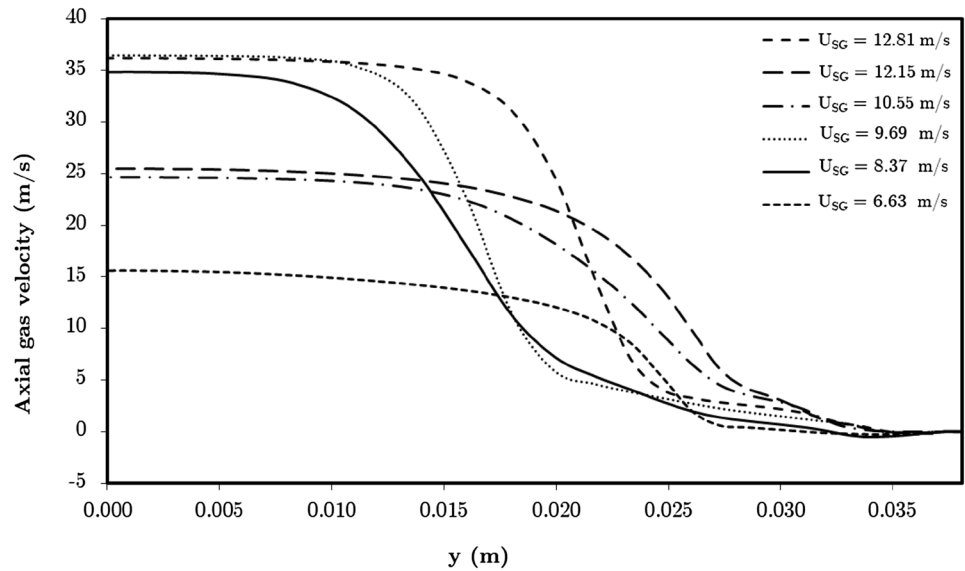
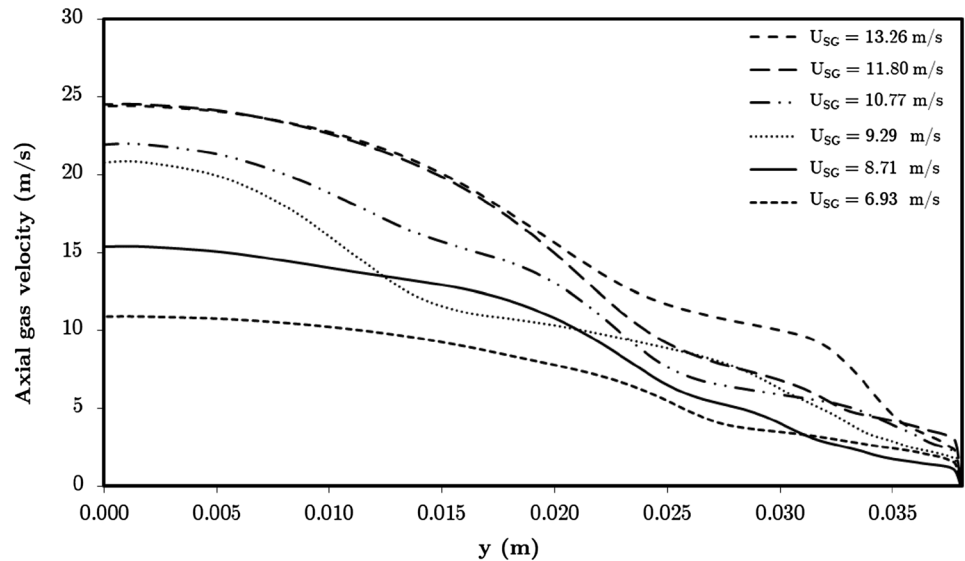


Fig. 31 Radial distribution of the axial gas velocity at section $x = 35D$ for cases of $U_{SL} = 0.1$ m/s



model should be carefully evaluated before performing the study.

- A further improvement in the boundary conditions is possible. The problem configuration that allows film reversal and results in the entire computational domain to resemble the actual case is highly recommended. For example, instead of injecting the liquid within a height of $5D$, it is recommended to inject the liquid uniformly over the entire pipe wall.
- The interface can be captured more accurately by using the Geo-reconstruction scheme for constructing the interface. The implementation of this scheme is only possible when using an explicit discretization with a smaller time step that meets the stability criteria and leads to convergence.

Fig. 32 Radial distribution of the axial gas velocity at section $x=35D$ for cases of $U_{SL}=0.05$ m/s

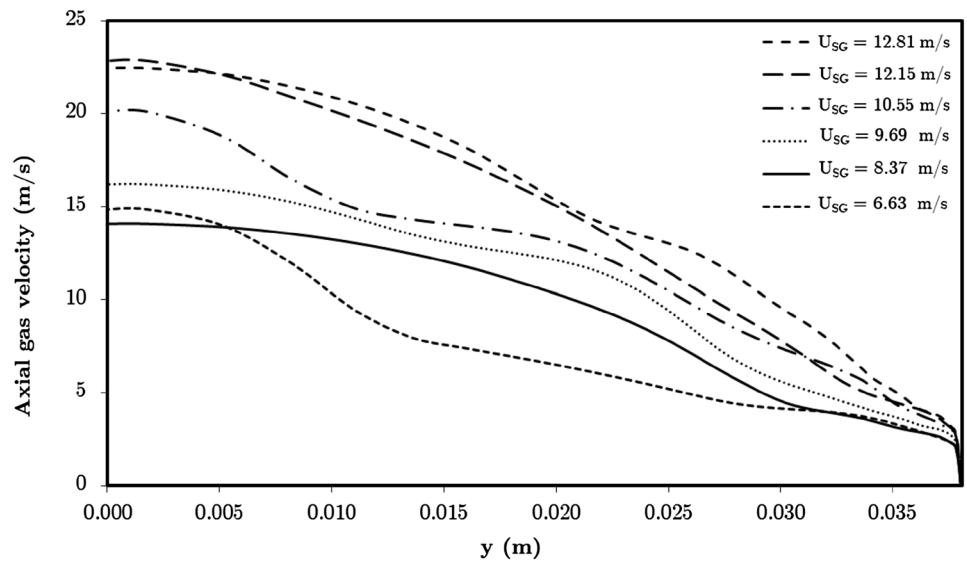


Fig. 33 Radial distribution of the axial gas velocity at section $x=35D$ for cases of $U_{SL}=0.01$ m/s

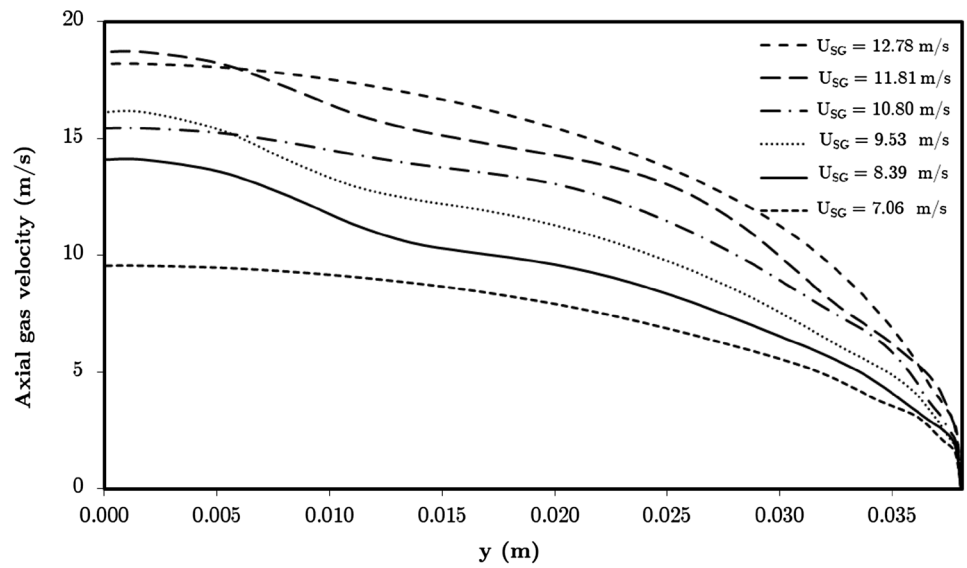


Fig. 34 Radial distribution of the axial liquid velocity at section $x = 12.5D$ for cases of $U_{SL} = 0.1$ m/s

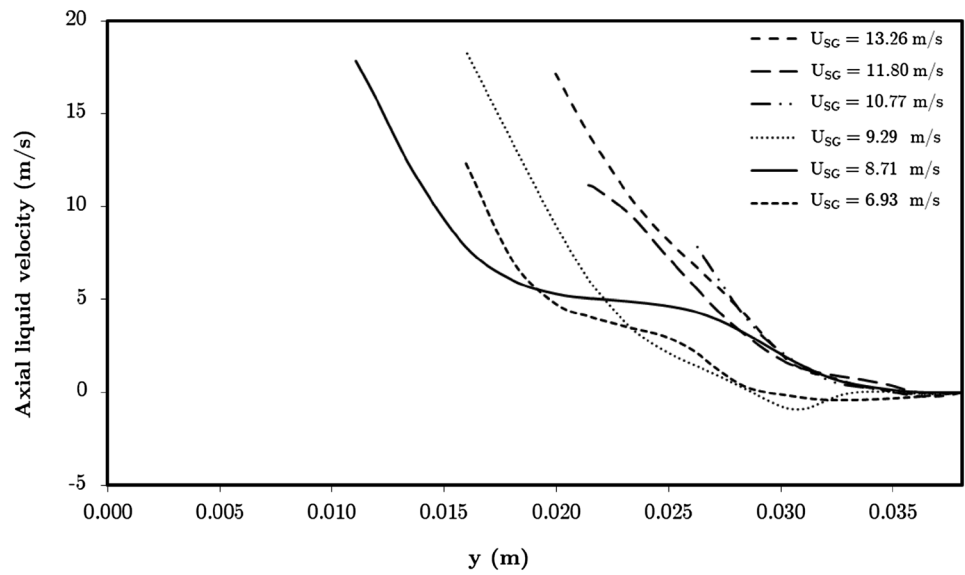


Fig. 35 Radial distribution of the axial liquid velocity at section $x = 12.5D$ for cases of $U_{SL} = 0.05$ m/s

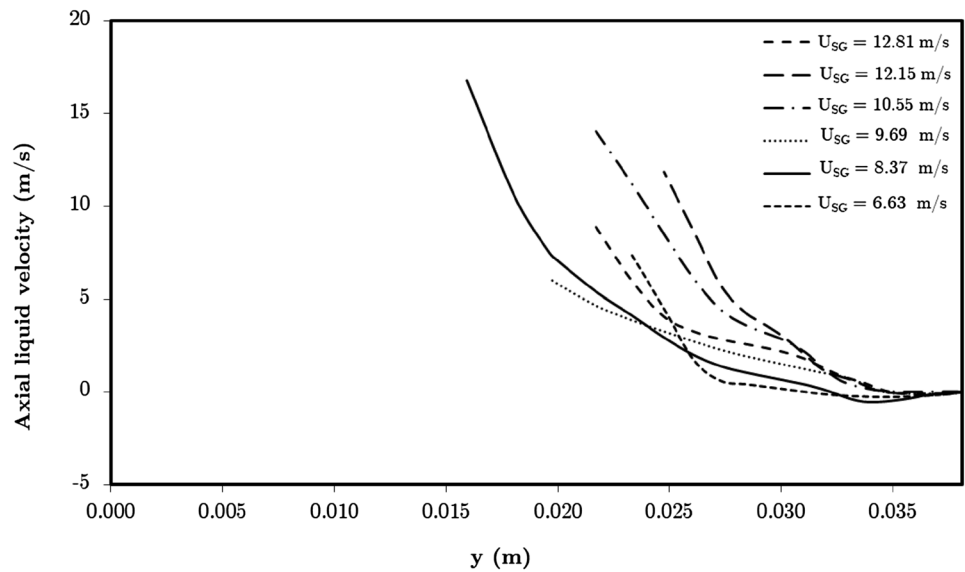


Fig. 36 Radial distribution of the axial liquid velocity at section $x=12.5D$ for cases of $U_{SL}=0.01$ m/s

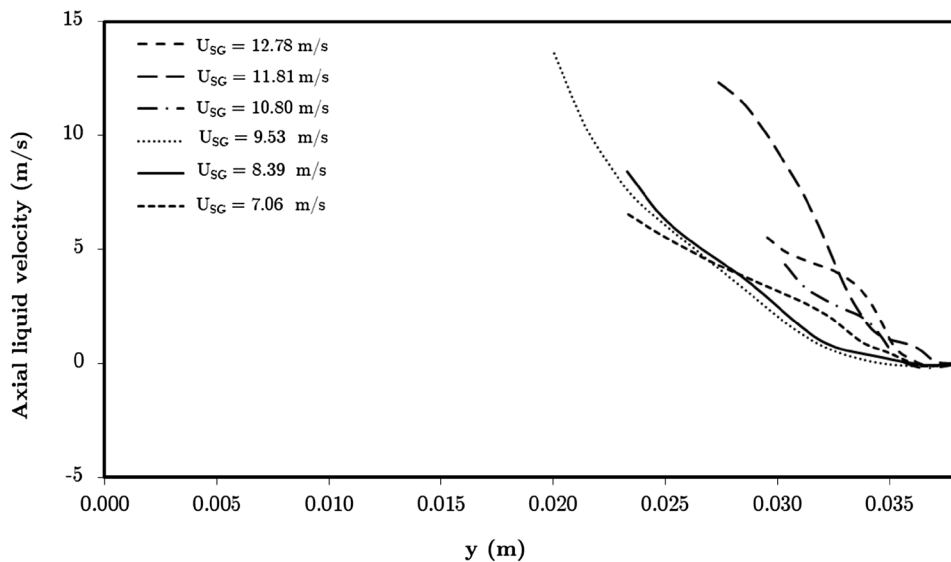


Fig. 37 Radial distribution of the axial liquid velocity at section $x=35D$ for cases of $U_{SL}=0.1$ m/s

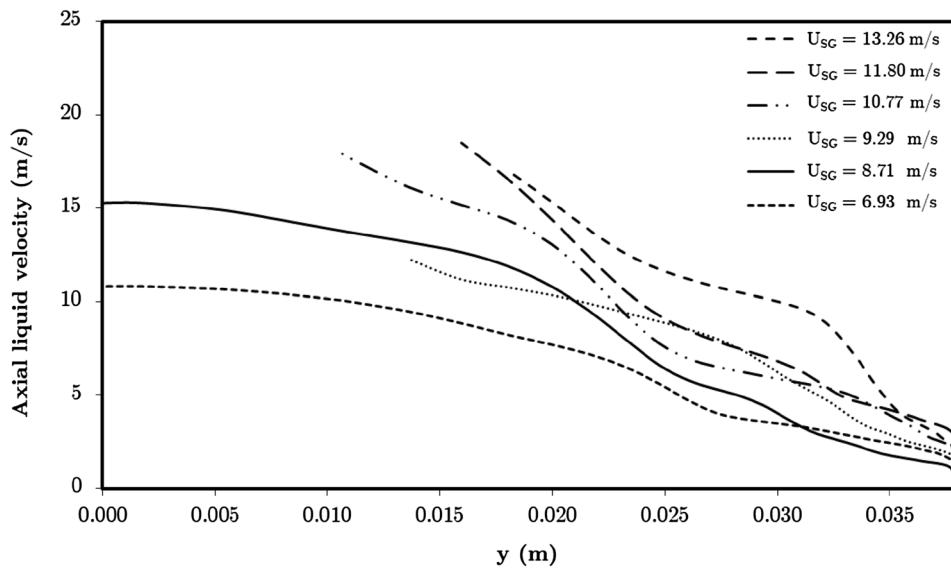


Fig. 38 Radial distribution of the axial liquid velocity at section $x=35D$ for cases of $U_{SL}=0.05$ m/s

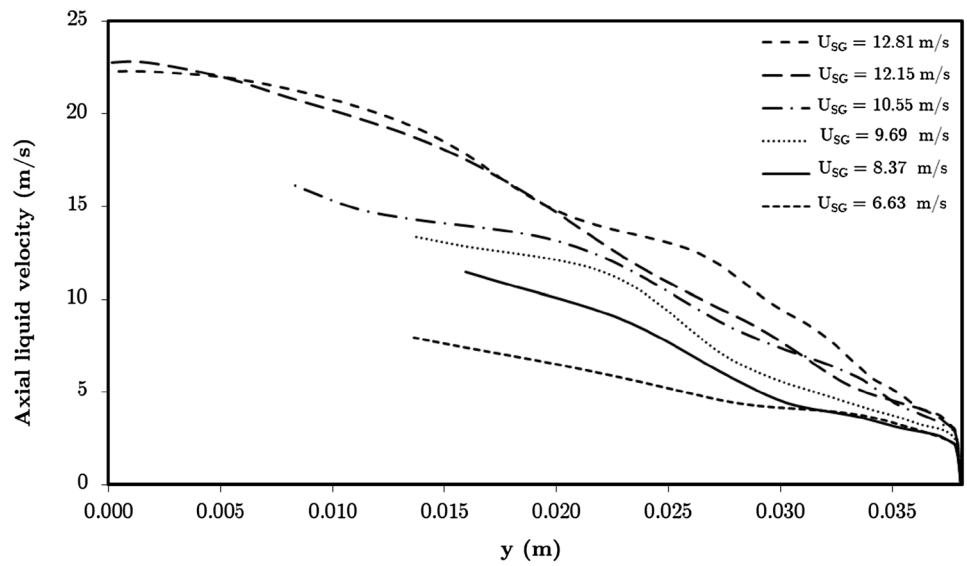


Fig. 39 Radial distribution of the axial liquid velocity at section $x=35D$ for cases of $U_{SL}=0.01$ m/s

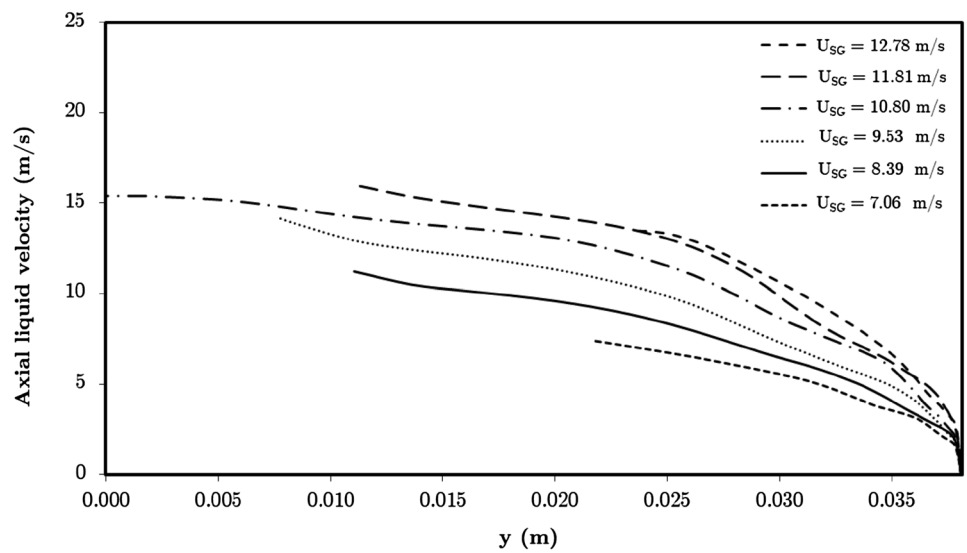


Fig. 40 Liquid wall shear stress fluctuation over time at section $x=12.5D$ for the case of $U_{SL}=0.1$ m/s and $U_{SG}=13.92$ m/s

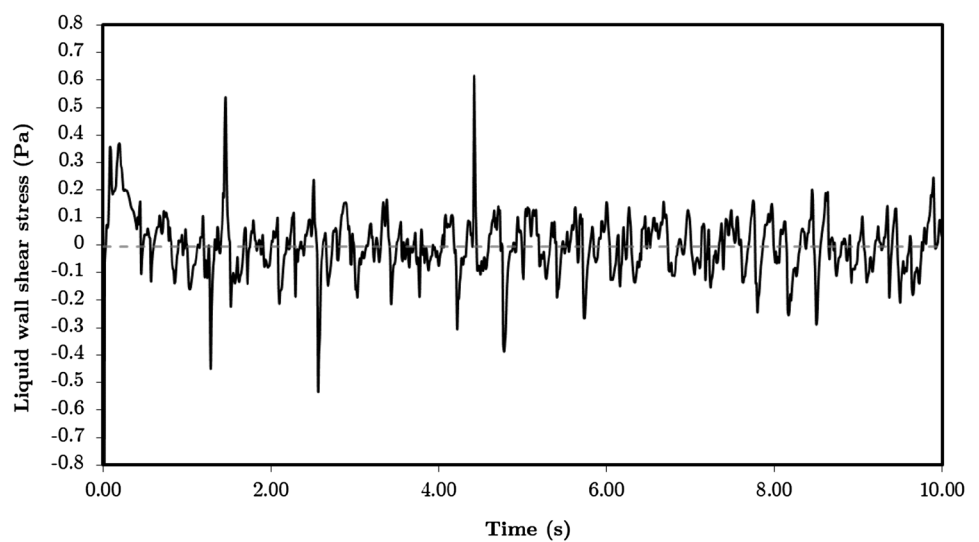


Fig. 41 Liquid wall shear stress fluctuation over time at section $x=12.5D$ for the case of $U_{SL}=0.05$ m/s and $U_{SG}=14.58$ m/s

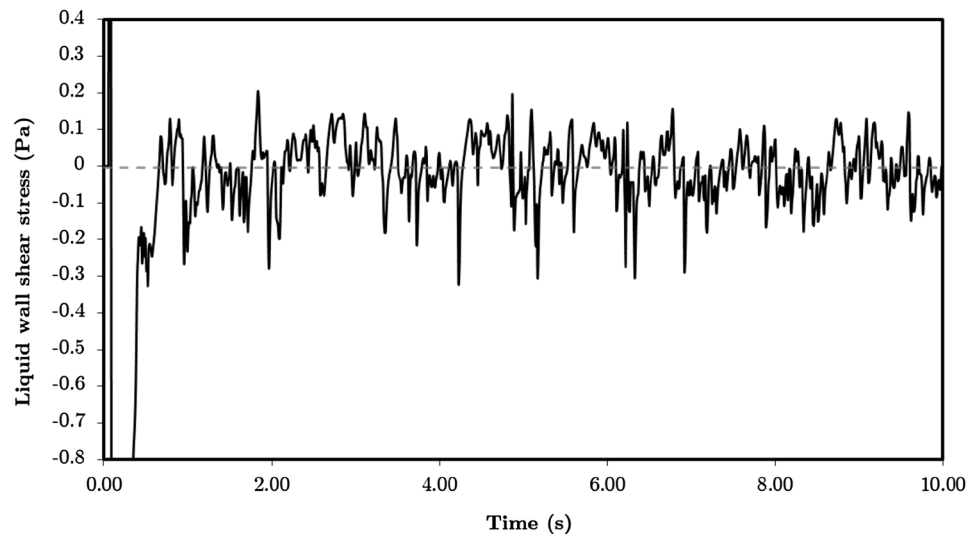
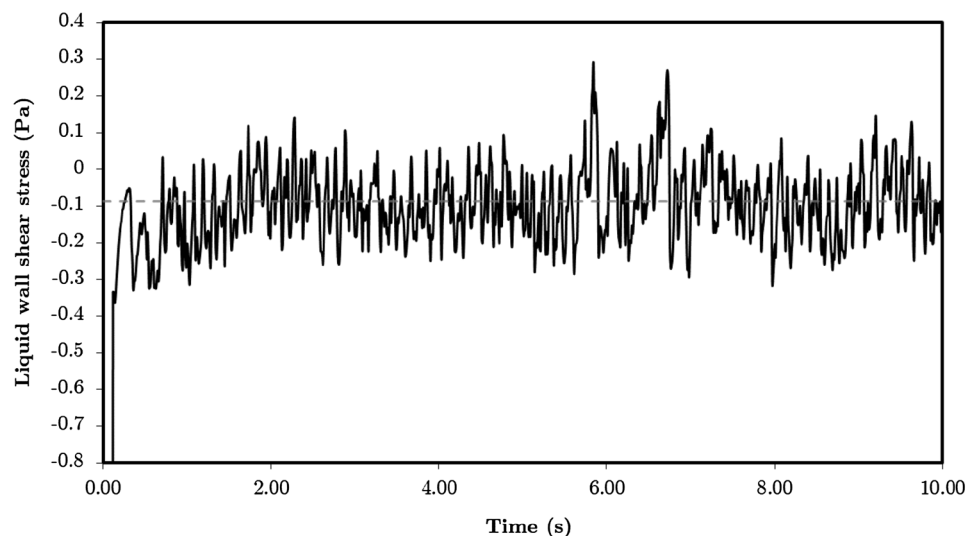


Fig. 42 Liquid wall shear stress fluctuation over time at section $x=12.5D$ for the case of $U_{SL}=0.01$ m/s and $U_{SG}=15.79$ m/s



- Sufficient refinement of the computational mesh in the core region and near the interface might result in a more accurate modeling of the liquid droplets entrained in the gas core. Here, due to the computational time limitation, the elements are coarse within the core region.
- The current study can also be expanded to include inclined pipes with different deviations in order to study the effect of the deviation angle on the flow field.

Open Access This article is distributed under the terms of the Creative Commons Attribution 4.0 International License (<http://creativecommons.org/licenses/by/4.0/>), which permits unrestricted use, distribution, and reproduction in any medium, provided you give appropriate credit to the original author(s) and the source, provide a link to the Creative Commons license, and indicate if changes were made.

References

- Adazev E (2018) Two-phase annular flow in vertical pipes. King Fahd University of Petroleum and Minerals
- Alipchenkov VM, Nigmatulin RI, Soloviev SL, Stonik OG, Zaichik LI, Zeigarnik YA (2004) A three-fluid model of two-phase dispersed-annular flow. *Int J Heat Mass Transf* 47(24):5323–5338
- Alsaadi Y, Pereyra E, Torres C, Sarica C (2015) Liquid loading of highly deviated gas wells from 60° to 88°. In SPE annual technical conference and exhibition
- Anderson TB, Jackson R (1967) A fluid mechanical description of fluidized beds. *Eng Chem Fundam* 6(4):527–539
- Ansys Inc (2009) ANSYS FLUENT 12.0 Theory guide
- Barnea D (1987) A unified model for predicting flow-pattern transitions for the whole range of pipe inclinations. *Int J Multiph Flow* 13:1–2
- Bartosiewicz Y, Laviéville J, Seynhaeve J-M (2008) A first assessment of the NEPTUNE_CFD code: instabilities in a stratified flow comparison between the VOF method and a two-field approach. *Int J Heat Fluid Flow* 29:460–478

- Belt R (2007) On the liquid film in inclined annular flow. Technical University Delft
- Bolajo EO, Fadairo AS, Ako CT, Omodara OJ, Emetere ME (2017) A new model for predicting liquid loading in multiphase gas wells. *Int J Appl Eng Res* 12:4578–4586
- Bowen RM (1976) Theory of mixture. *Contin Phys* 3:2–129
- Brackbill J, Kothe D, Zemach C (1992) A continuum method for modeling surface tension. *J Comput Phys* 100(2):335–354
- Chen J, Tang Y, Zhang W, Wang Y, Qiu L, Zhang X (2015) Computational fluid dynamic simulations on liquid film behaviors at flooding in an inclined pipe. *Chin J Chem Eng* 23(9):1460–1468
- Coleman SB, Clay HB, McCurdy DG, Norris LH (1991) A new look at predicting gas-well load-up. *J Pet Technol* 43(03):329–333
- Fadairo A, Olugbenga F, Sylvia NC (2015) A new model for predicting liquid loading in a gas well. *J Nat Gas Sci Eng* 26:1530–1541
- Govan AH (1990) Modelling of vertical annular and dispersed two-phase flows. University of London
- Guner M (2012) Liquid loading of gas wells with deviations from 0° to 45°. The University of Tusla
- Guner M, Pereyra E, Sarica C, Torres C (2015) An experimental study of low liquid loading in inclined pipes from 90° to 45°. In SPE production and operations symposium
- Guo B, Ghalambor A, Xu C (2005) A systematic approach to predicting liquid loading in gas wells. In SPE production operations symposium
- Han C (2005) Huawei (University of Saskatchewan) A study of entrainment in two-phase upward cocurrent annular flow in a vertical tube
- Han H, Gabriel K (2007) A numerical study of entrainment mechanism in axisymmetric annular gas-liquid flow. *J Fluids Eng* 129:293–301
- Jayanti S, Hewitt GF (1997) Hydrodynamics and heat transfer in wavy annular gas-liquid flow: a computational fluid dynamics study. *Int J Heat Mass Transf* 40(10):2445–2460
- Karami H, Torres CF, Parsi M, Pereyra E, Sarica C (2014) CFD Simulations of Low Liquid Loading Multiphase Flow in Horizontal Pipelines. *Fora: Cavitation and Multiphase Flow; Fluid Measurements and Instrumentation; Microfluidics; Multiphase Flows: Work in Progress; Fluid-Particle Interactions in Turbulence*, vol 2, p V002T06A011
- Kishore BN, Jayanti S (2004) A multidimensional model for annular gas-liquid flow. *Chem Eng Sci* 59(17):3577–3589
- Li M, Lei S, Li S (2001) New view on continuous-removal liquids from gas wells. In SPE Permian basin oil and gas recovery conference
- Liu Y, Cui J, Li WZ (2011) A two-phase, two-component model for vertical upward gas-liquid annular flow. *Int J Heat Fluid Flow* 32(4):796–804
- Nosseir MA, Darwich TA, Sayyoub MH, El Sallaly M (1997) A new approach for accurate prediction of loading in gas wells under different flowing conditions. In SPE production operations symposium
- Stevanovic V, Studovic M (1995) A simple model for vertical annular and horizontal stratified two-phase flows with liquid entrainment and phase transitions: one-dimensional steady state conditions. *Nucl Eng Des* 154(3):357–379
- Taitel Y, Bornea D, Dukler AE (1980) Modelling flow pattern transitions for steady upward gas-liquid flow in vertical tubes. *AIChE J* 26(3):345–354
- Turner RG, Hubbard MG, Dukler AE (1969) Analysis and prediction of minimum flow rate for the continuous removal of liquids from gas wells. *Pet Trans AIME* 21(11):1475–1482
- van't Westende JMC, Kemp HK, Belt RJ, Portela LM, Mudde RF, Oliemans RVA (2007) On the role of droplets in cocurrent annular and churn-annular pipe flow. *Int J Multiph Flow* 33(6):595–615
- Vieiro J, Asuaje M, Polanco G (2013) Study of the two-phase liquid loading phenomenon by applying CFD techniques. *Int J Multiphys* 7(4):301–313
- Yan L, Wang Y, Wu Z, Dai Z, Yu G, Wang F (2017) Research of vertical falling film behavior in scrubbing-cooling tube. *Chem Eng Res Des* 117:627–636
- Zabaras G, Dukler AE, Moalem-Maron D (1986) Vertical upward cocurrent gas-liquid annular flow. *AIChE J* 32(5):829–843
- Zhou D, Yuan H (2010) A new model for predicting gas-well liquid loading. *SPE Prod Oper* 25(02):172–181

Publisher's Note Springer Nature remains neutral with regard to jurisdictional claims in published maps and institutional affiliations.